


Article

Two-Stage Orogenic Cycle of the Eastern Paleo-Asian Ocean from Early Palaeozoic to Early Triassic: Constraints from Magmatic Rocks of the Southeastern Central Asian Orogenic Belt

Jinlei Sun ^{1,2} , Ye Qian ^{1,3,*}, Jinyu Li ⁴, Yanjie Shen ¹, Lixiang Zhao ¹ and Fegnyue Sun ¹¹ College of Earth Sciences, Jilin University, No. 2199, Jianshe Street, Changchun 130061, China² State Key Laboratory of Ore Deposit Geochemistry, Institute of Geochemistry, Chinese Academy of Sciences, Guiyang 550081, China³ Key Laboratory of Mineral Resources Evaluation in Northeast Asia, Ministry of Nature Resources of China, No. 2199, Jianshe Street, Changchun 130061, China⁴ State Key Laboratory of Geological Processes and Mineral Resources, China University of Geosciences, Wuhan 430074, China

* Correspondence: qianye@jlu.edu.cn



Citation: Sun, J.; Qian, Y.; Li, J.; Shen, Y.; Zhao, L.; Sun, F. Two-Stage Orogenic Cycle of the Eastern Paleo-Asian Ocean from Early Palaeozoic to Early Triassic: Constraints from Magmatic Rocks of the Southeastern Central Asian Orogenic Belt. *Minerals* **2022**, *12*, 1040. <https://doi.org/10.3390/min12081040>

Academic Editors: Mauro Cesar Geraldes, Alexandre Andronikov and Guilherme Loriato Potratz

Received: 18 June 2022

Accepted: 15 August 2022

Published: 19 August 2022

Publisher's Note: MDPI stays neutral with regard to jurisdictional claims in published maps and institutional affiliations.



Copyright: © 2022 by the authors. Licensee MDPI, Basel, Switzerland. This article is an open access article distributed under the terms and conditions of the Creative Commons Attribution (CC BY) license (<https://creativecommons.org/licenses/by/4.0/>).

Abstract: The evolution of the eastern Paleo-Asian Ocean (PAO) has controlled the formation of the southeastern Central Asian Orogenic Belt (CAOB). However, the evolution history and final closure time of the eastern PAO still remain controversial, which greatly restricts understanding of the formation process of the CAOB. To address these issues, we provide detailed zircon chronology and Hf isotope and geochemical data of Paleozoic to Triassic magmatic rocks in the southeastern CAOB. We have identified four periods of magmatism as evidenced by: Early Silurian quartz diorites (434.7 Ma), Early Devonian monzogranites (394.2 Ma), Middle Permian granites (260.2–264.5 Ma) and Late Permian–Early Triassic syenogranite (250.8–253.6 Ma). These rocks have features of low MgO and mantle-compatible elements, are enriched in Th, U, K, Pb, Sr, Zr and Hf and depleted in Nb, Ta, La, Ce, P, and Ti. The quartz diorites belong to the medium-K calc-alkaline series with $\epsilon\text{Hf}(t)$ values of -0.76 to 2.21 , indicating that they may be derived from partial melting of mafic lower crust with minor contribution of mantle magma. The monzogranites and syenogranite have high Zr + Nb + Ce + Y (260–390; 261–461 ppm, respectively), total alkali contents (9.98–10.80; 8.46–9.29 wt.%, respectively), and high zircon saturation temperature (807–840; 810–885 °C). They can be classified as A-type granites. Monzogranites have $\epsilon\text{Hf}(t)$ values (between -1.20 and $+3.34$); hence, we believe that they were derived from the crust modified by mantle-derived fluids or melts. Syenogranite have high $\epsilon\text{Hf}(t)$ values (5.49–11.36), and we suggest that they were derived from the juvenile lower crust that originated from the depleted mantle. The granites have high Sr/Y ratios (118–257), low Y (1.42–2.82 ppm), and Yb (0.31–0.41 ppm), consistent with the features of adakite. Considering the $\epsilon\text{Hf}(t)$ isotopic values (2.99–8.50), we suggest that they originated from thickened juvenile lower crust. Combining the results from our own and previous studies, we propose a new evolution model of the eastern PAO from Paleozoic to Triassic. It can be divided into two stages: (1) Late Cambrian to Early Devonian; (2) Early Permian to Triassic. The first stage is the evolution of the Bainaimiao ocean (secondary ocean basin of the PAO), which closed in the Late Silurian and led to the Bainaimiao arc accretion to the North China Cratons. The second stage is the final closure of the eastern PAO during the Late Permian (~254 Ma).

Keywords: Central Asian Orogenic Belt; Early Silurian to Early Triassic; Paleo-Asian Ocean

1. Introduction

Orogenic belts mainly include collisional orogenic belts, subduction accretionary orogenic belts and intracontinental orogenic belts [1–5]. The subduction and closure of an

ocean can produce accretionary orogenic belts, which mainly include accretionary wedges, oceanic plateaus, island arcs, back-arc basins, etc. [6]. The mechanism of orogenic accretion has since long been the focus of attention [7,8]. The Central Asian Orogenic Belt (CAOB) is the largest and longest accretionary orogenic belt on the Earth, and it is adjacent to the Siberian craton in the North and the Tarim and North China Cratons (NCC) in the south (Figure 1a) [9,10]. Its formation and evolution are the results of amalgamation of different island arcs, oceanic island, and micro-continents from the Mesoproterozoic to the Late Paleozoic, and are closely related to opening, subduction-accretion, and closure of the Paleo-Asian Ocean (PAO) [8,11–13]. Therefore, clarifying the evolution of the PAO will be very important for understanding the accretion mechanisms of the CAOB.

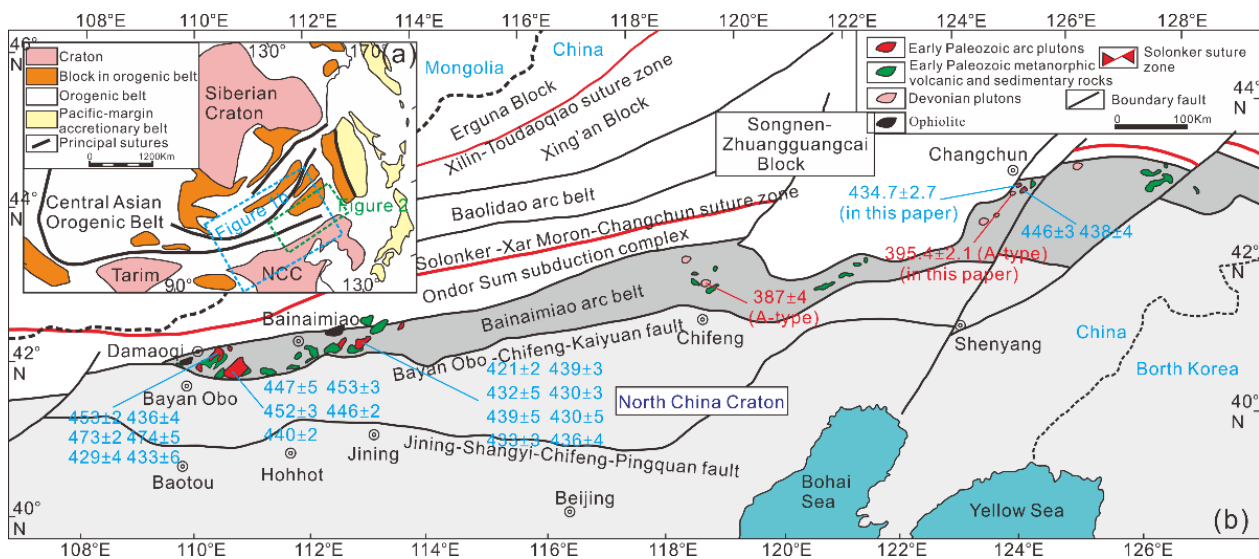


Figure 1. (a) Simplified tectonic sketch map of the southeastern CAOB and (b) the northern margin of the Northeast China block. Age data and references presented in supplementary material Table S1.

Previous studies show that the breakup of the supercontinent Rodinia has led to the opening of the PAO in the Neoproterozoic (~1.0 Ga) [11]. Recently, more and more studies have shown that the PAO experienced double-sided subduction directed southward and northward [12–16]. The PAO changed from the subduction accretion to the collision stage in the Paleozoic, and its closure has followed a scissor-like pattern from west to east [2–4,17,18]. The PAO was closed in the Late Carboniferous in the Tarim area on the southern margin of the CAOB [15,16] and closed in Early-Middle Permian on the Northern margin of the Alxa block in the western NCC [18]. However, the evolution of the eastern PAO in the southeastern CAOB is still controversial. There is no consensus about the evolution of the eastern PAO from the Paleozoic to the Early Triassic, especially its final closure time [8,18]. Based on the presence of Late Devonian metamorphic rocks and the extension-related magmatic activity of the Carboniferous, some scholars believe that the final closure of the eastern PAO occurred in the Devonian to Carboniferous, which led to the formation of the Bainaimiao arc belt (Figure 1b) [19–21]. However, this interpretation does not account for the abundance of arc-related magmatic activity from the Permian to the Triassic times. Other investigators believe that the final closure happened during the Late Paleozoic to Early Mesozoic [22–24], but they do not have a detailed understanding of the timing of events. Obviously, the evolution of the eastern PAO needs further study.

During oceanic subduction and ocean closure, a large number of magmatic rocks are usually produced, which can provide a key window for studying the evolution of the ocean. In the southeast CAOB, there are many Paleozoic to early Mesozoic magmatic rocks distributed from west to east [12,22–25], and they are closely related to the evolution of the eastern PAO in time and space, so they are records of the evolution of the eastern PAO. A combined petrological, geochronological, and geochemical study of these rocks can provide

important information to solve the evolution issues of the eastern PAO. Here, we provide detailed whole-rock geochemistry, zircon geochronology and Hf isotopic composition of Paleozoic to Early Triassic rocks in the southeastern CAOB, in the attempt to clarify the evolutionary history and final closure time of the eastern PAO.

Geological Setting and Sample Descriptions

Northeast (NE) China is an important part of the southeast CAOB, and it mainly consists of micro-continental blocks and island arcs, including the Erguna, Xing'an and Songnen-Zhangguangcai blocks, the Baolidao arc and Bainaimiao arc belts, etc. (Figure 1b) [9,14]. Some suture zones and tectonic faults have been identified in NE China, such as the Ji'ning-Shangyi-Chifeng-Pingquan fault, the Bayan Obo-Chifeng-Kaiyuan fault, and the Solonker-Xar Moron-Changchun suture zone (Figure 1b) [12,18]. Many studies show the Erguna and Xing'an blocks' amalgamation along the Xilin-Toudaoqiao fault in the Early Paleozoic (Figure 1b) [26,27], and the Solonker-Xar Moron-Changchun suture zone formed by the closure of the eastern PAO, although the time of collision is controversial [17,18]. The closure times under discussion mainly are Devonian-Carboniferous and Late Permian to Middle Triassic [28–32].

The Bainaimiao arc is situated in the north of the NCC and in the south of the Solonker-Xar Moron-Changchun suture zone (Figure 1b). It is mainly composed of Paleozoic arc complexes, formed between the Middle Silurian and the Late Cambrian, and includes diorite, amphibolite, granodiorite, and granite [12,17]. There are also a small number of metamorphic volcanic and sedimentary rock assemblages distributed along the margin of magmatic arc rocks. In addition, the strata in the Bainaimiao area consist of the Cambrian-Ordovician Bainaimiao Group, the Silurian Xuniwusu and the Xibiehe Formation (Fm). The Bainaimiao Group is essentially a set of metamorphic volcanic sedimentary rocks and unconformable with the Xuniwusu Fm. The Xuniwusu Fm consists mainly of low-grade metamorphic marine clastic limestone and dacitic tuff, that are covered unconformably by Xibiehe Fm. The Xibiehe Fm is a set of conglomerates, shallow marine clastic and carbonate sedimentary assemblages, which are typical of molasse depositions [21].

The study area is located in the central Jilin Province, southeastern CAOB. The strata mainly include Early Paleozoic, Cretaceous, Jurassic, and Quaternary strata (Figures 2 and 3). The Early Paleozoic strata consist of Ordovician volcanic strata, Silurian Taoshan and Wanyue Fm. The lower part of the Ordovician volcanic strata is gray green dacitic breccia tuff, and the upper part is dominated by foliated dacitic tuff and tuffaceous sandstone [33,34]. The lithology consists of sandstones of the Taoshan Fm and foliated rhyolite of the Wanyue Fm, respectively [34–36]. The Jurassic strata are represented by the Anmin Fm, which is composed of intermediate-acid volcanic rocks, andesite and dacite. The Cretaceous strata are made up of the Quantou Fm, which is composed of brownish red conglomerate and sandstone, and purplish red argillaceous siltstone [34]. The Quaternary is exposed along the banks of rivers. The study area has been affected by the PAO and Paleo-Pacific Ocean, resulting in frequent magmatic activities from the Paleozoic to the Mesozoic. Rocks range from mafic to felsic and are exposed over more than 100 km² (Figure 2; Supplementary Material Table S1) [37]. Among them, the rocks related to the PAO mainly developed in the Late Paleozoic to Triassic. For our study we sampled fresh quartz diorite (Y2001), monzogranite (Y2002), granite (Y2046, Y2047) and K-feldspar granite (Y2058, Y2059) in the Nanweizi, Taipingling, and Shoushan areas (Figure 3), Jilin Province, for detailed petrographic analyses.

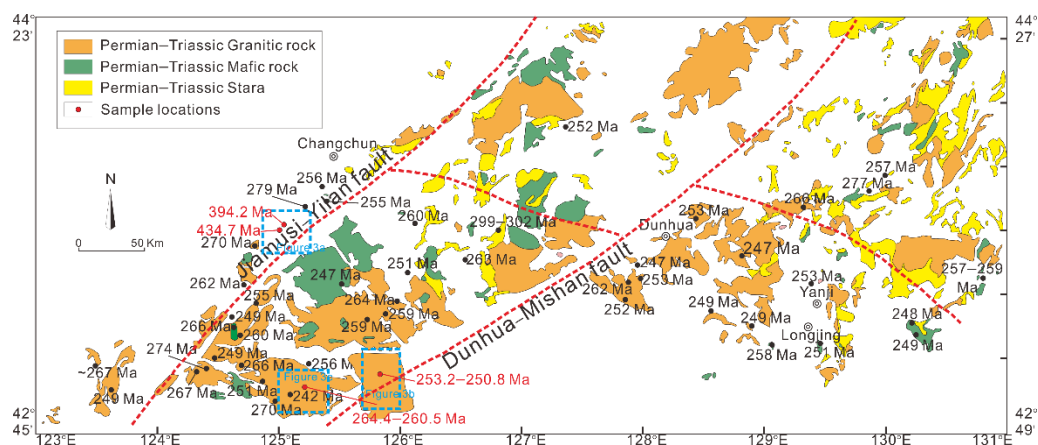


Figure 2. Distribution of the Permian to Triassic magmatic rocks in the central Jilin Province, southeastern CAOB. Figure 3a–c marked in the figure is the location of the study area in this paper. Age data and references presented in Supplementary Material Table S1.

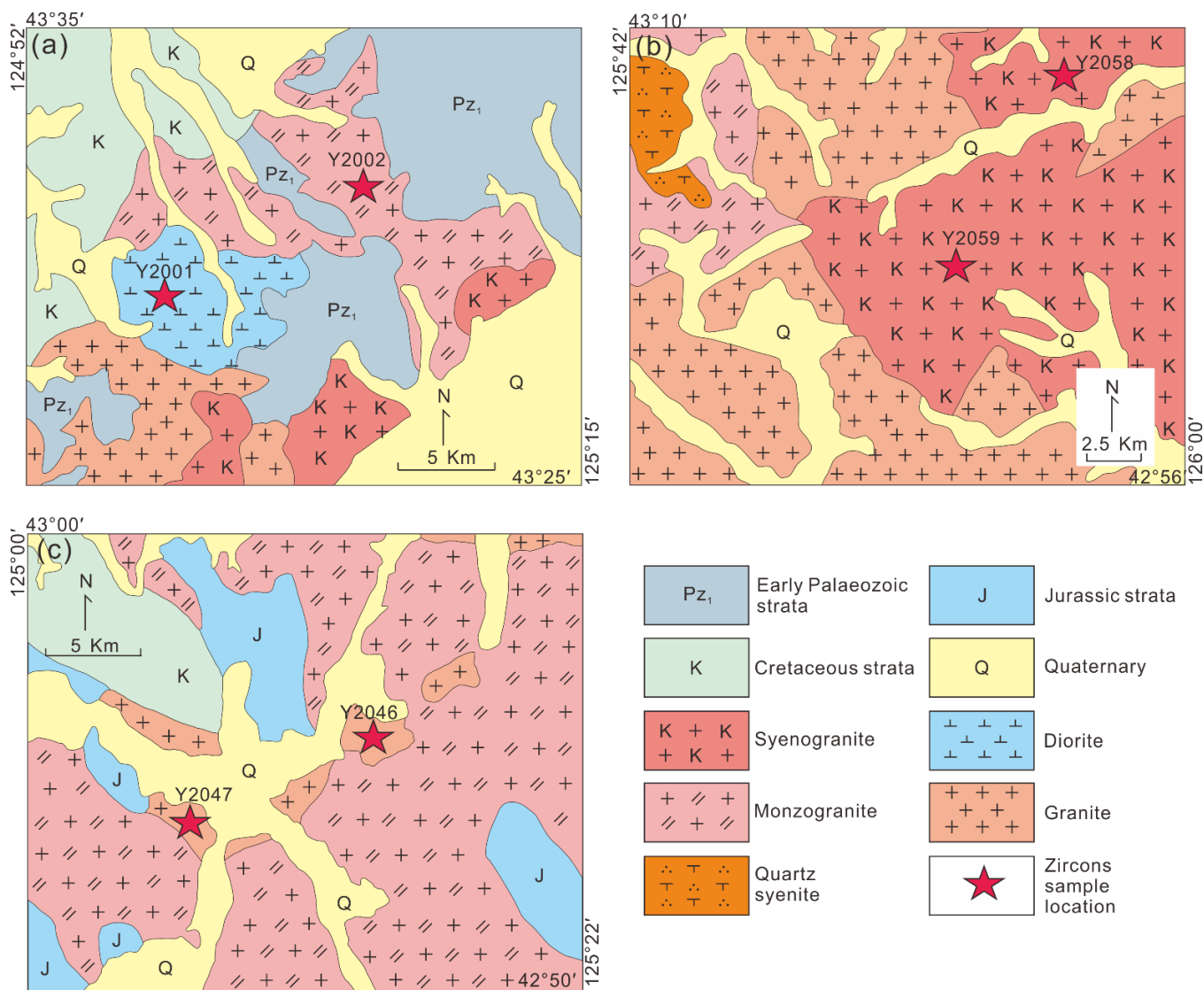


Figure 3. Detailed geological map of the (a) Nanweizi, (b) Taipinling, and (c) Shoushan area in the central Jilin Province, showing the zircon sample locations.

All samples are massive, with a medium-coarse grained granitic texture (Figure 4). The quartz diorites consist of plagioclase (60%–65%), hornblende (~15%), quartz (~10%), and biotite (~10%). The monzogranites are composed of quartz (~20%), plagioclase (35%–40%), K-feldspar (~35%), and minor hornblende and biotite (~5%). The granites consist of plagioclase (30%–35%), K-feldspar (30%–35%), quartz (20%–25%), and biotite (~5%). The syenogranite contains perthitic K-feldspar (55%–60%), quartz (~30%) and plagioclase (~10%). In addition, some accessory minerals are present in the samples, including zircon, apatite and titanite.

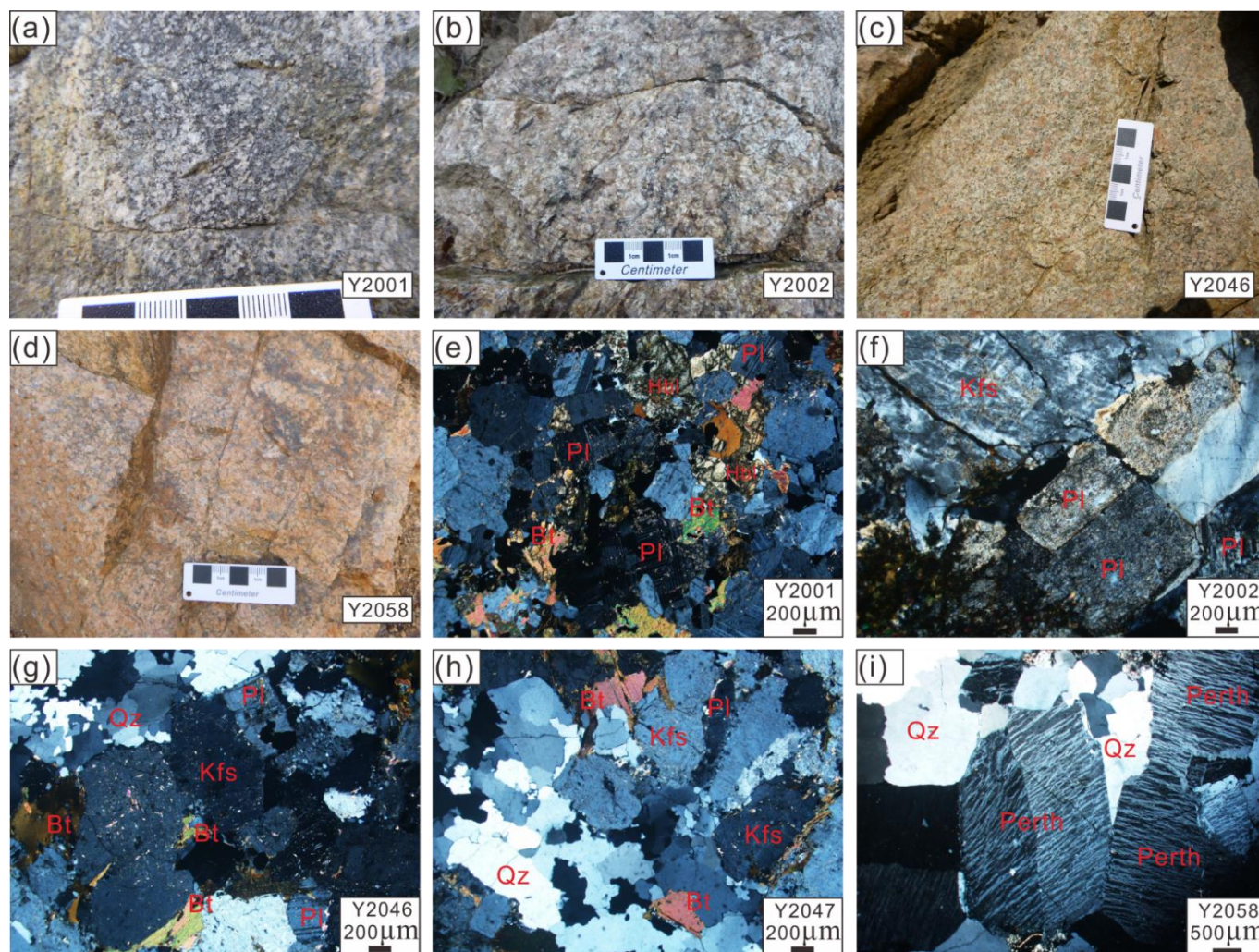


Figure 4. Field photographs (a–d) and photomicrographs (e–i) showing typical features of the analyzed samples. (a) quartz diorite (Y2001); (b) monzogranite (Y2002); (c) granite (Y2046) and (d) syenogranite (Y2058). (e–i) cross polarized light. Kfs: K-feldspar; Pl: plagioclase; Qz: quartz; Bt: biotite; Hbl: hornblende; Perth: perthite.

2. Analytical Methods

Zircon U-Pb dating, major- and trace-element analyses were carried out at the Key Laboratory of Mineral Resources Evaluation in Northeast Asia, Ministry of Nature Resources of China, Changchun.

2.1. Zircon U-Pb Dating

Zircons from six samples were separated by magnetic and heavy-liquid separation techniques at the Langfang Regional Geological Survey, Hebei Province, China. The internal structure of zircon was revealed by transmitted light and cathodoluminescence

(CL) images. U-Pb ages of zircons were determined using an Agilent 7900 ICP-MS with 193 nm ArF excimer laser system (LA). The beam diameter was 32 μm , with a frequency of 8 Hz and laser energy of 60 J/cm². Helium was used as carrier gas. Zircon 91500 was adopted as the external standard for age calibration and NIST610 silicate glass was used to quantify trace-element concentrations. The detailed procedures of the test were described by Liu et al. [38]. The ICP-MS DataCal [38] and Isoplot3 program [39] were used for age data processing. Common Pb corrections are based on Andersen's [40] method.

2.2. Major and Trace Element Analyses

Thirteen samples were analyzed for whole-rock major and trace elements. Major elements were measured by X-ray fluorescence (XRF) using fused glass disks. After removing the weathering surfaces, samples were smashed to 200-mesh size. The sample powder (0.8 g) and lithium borate flux (8 g) were mixed well, transferred to a platinum crucible and melted at 1050 °C. Subsequently, the melt was cooled to form a glass disk that was used for XRF analysis. Trace elements were analyzed by Agilent 7500a ICP-MS. The samples were dissolved in 2 mL acid mixture (1:1 HF + HNO₃) in a Teflon bomb and dried at 140 °C on an electric heating plate. 2 mL acid mixture was added, followed by place in a 190 °C oven for 48 h. The sample was dried again, 2 mL HNO₃ acid was added and placement in a 150 °C oven for 12 h. The sample was finally made into an aqueous solution for analysis. The accuracy of analyses was monitored using China national standard GBW07103 and GBW07105. The error is less than 5% for major elements and 10% for trace elements.

2.3. Zircon Hf Isotopic Analyses

Six zircon samples were chosen for Hf isotopic analyses. The analyses were carried out using a Neptune plus MC-ICP-MS with a 193 nm ArF excimer laser system at the National Research Center of Geoanalysis, Beijing. The ablation protocol employed a spot diameter of 50 μm with repetition rate of 10 Hz and laser energy of ~ 7 J/cm². The zircons PLE, Qinghu, and 91,500 were selected as standards for precision control. The details of the testing steps and calibration methods are given by Wu et al. [41] and Guo et al. [42].

3. Analytical Results

3.1. Zircon U-Pb Ages and Hf Isotopic Composition

Zircon U-Pb ages and Hf isotopic compositions are listed in supplementary material Tables S2 and S3. Internal structures of zircons are shown in Figure 5. The morphology of zircon grains is mainly subhedral to euhedral, with 80–150 μm in length. All zircons display typical oscillatory growth zoning and high Th/U ratios (0.12–1.41), suggesting an igneous origin [43].

Twenty zircons from sample Y2001 (quartz diorite) show ²⁰⁶Pb/²³⁸U ages between 431.2 and 438.3 Ma, with a weighted mean age of 434.7 ± 2.7 Ma, i.e., Early Silurian (Figure 6a). Ten zircon crystals yield $\epsilon\text{Hf}(t)$ values of -0.76 to $+2.21$ (Figure 7).

Twenty-one zircons from sample Y2002 (monzogranite) yield ²⁰⁶Pb/²³⁸U ages from 391.4 to 398.9 Ma, with a weighted mean age of 394.2 ± 2.1 Ma, i.e., Early Devonian (Figure 6b). Eleven zircon grains have $\epsilon\text{Hf}(t)$ values of -1.20 to $+3.34$ (Figure 7).

Sixteen zircons from Y2046 (granite) show ²⁰⁶Pb/²³⁸U ages vary from 258.2 to 263.4 Ma, with a weighted mean age of 260.2 ± 2.4 Ma, i.e., Middle Permian (Figure 6c). Ten zircon crystals yield $\epsilon\text{Hf}(t)$ values of 2.99 to 8.01 (Figure 7).

Twenty zircons from Y2047 (granite) show ²⁰⁶Pb/²³⁸U ages varying between 260.3 and 267.2 Ma, with a weighted mean age of 264.5 ± 2.2 Ma, i.e., Middle Permian (Figure 6d). Nine zircon crystals yield $\epsilon\text{Hf}(t)$ values of 3.22 to 8.50 (Figure 7).

Twenty-one zircons from Y2058 (syenogranite) show ²⁰⁶Pb/²³⁸U ages ranging from 251.2 to 256.0 Ma, with a weighted mean age of 253.6 ± 1.6 Ma, i.e., Late Permian (Figure 6e). Nine zircon crystals yield $\epsilon\text{Hf}(t)$ values of 6.54 to 11.36 (Figure 7).

Seventeen zircons from Y2059 (syenogranite) show $^{206}\text{Pb}/^{238}\text{U}$ ages that vary between 248.0 and 253.6 Ma, with a weighted mean age of 250.8 ± 1.8 Ma, i.e., Early Triassic (Figure 6f). Ten zircon crystals yield $\epsilon\text{Hf}(t)$ values of 5.49 to 10.43 (Figure 7).

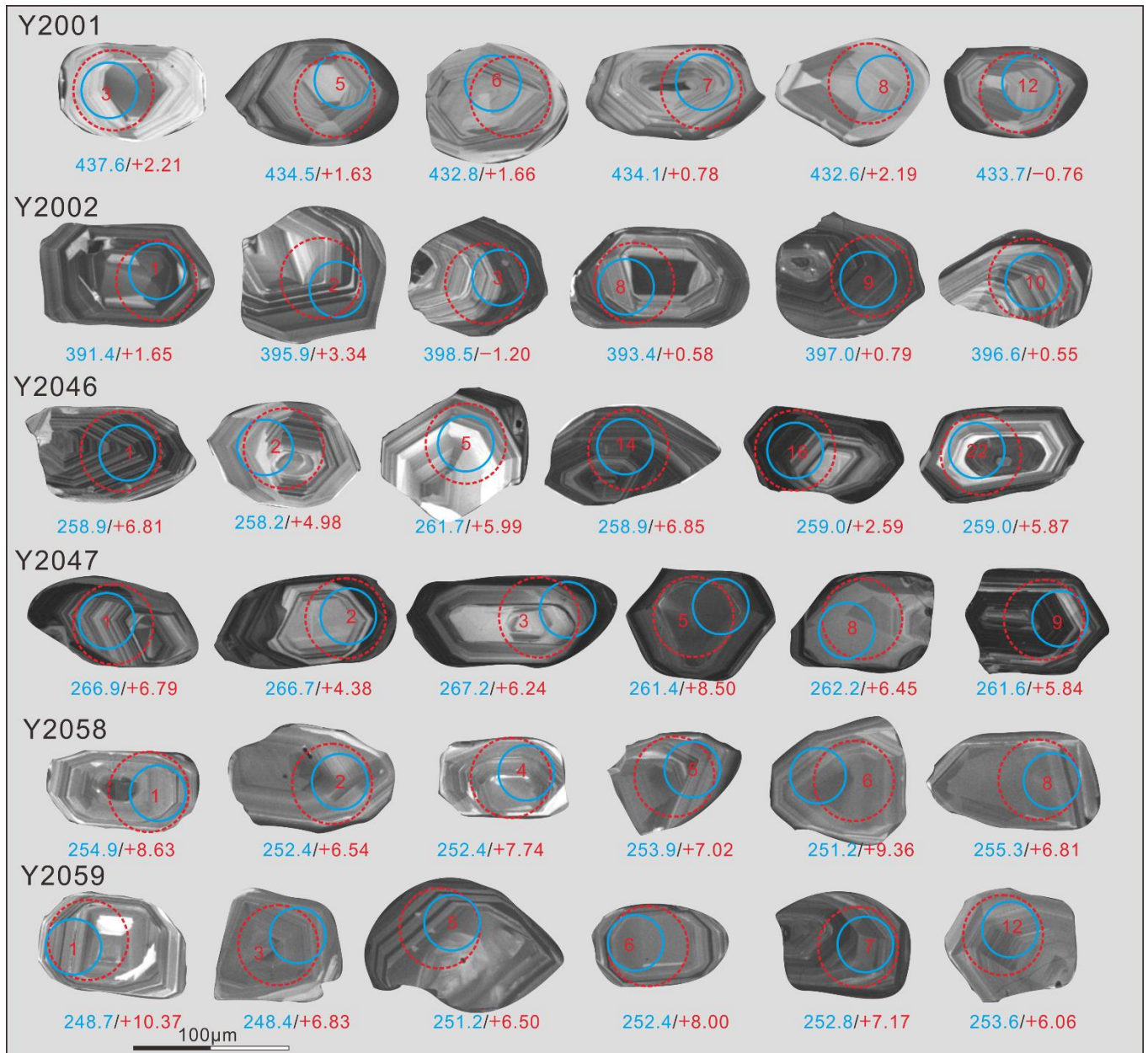


Figure 5. CL images, zircon U–Pb ages (in Ma) and $\epsilon\text{Hf}(t)$ isotopic compositions for the analyzed zircon samples. Cyan and red circles represent the locations of U–Pb age and Hf isotope analyses, respectively.

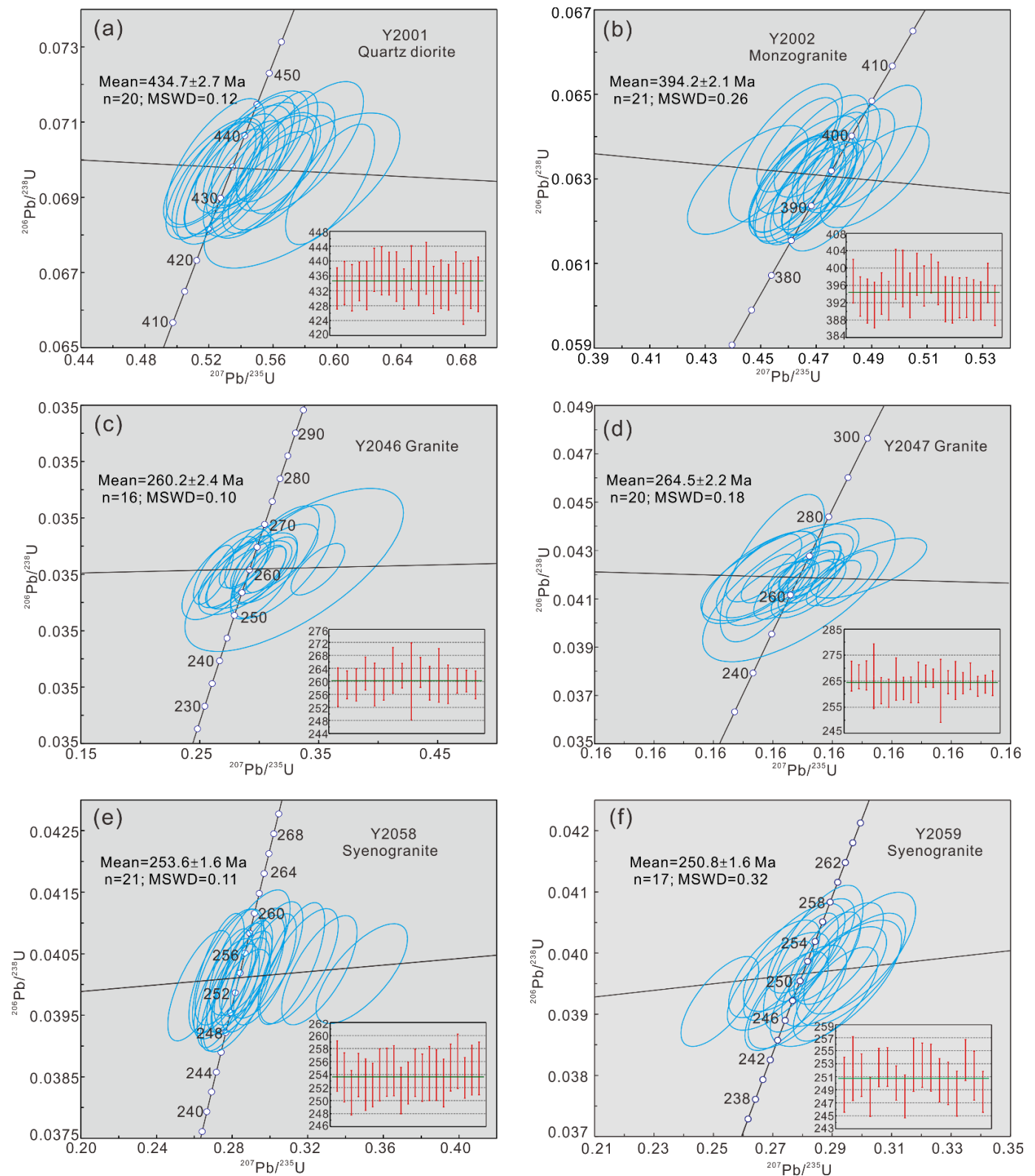


Figure 6. U-Pb concordia diagrams and weighted mean age for zircons from analyzed samples. (a) quartz diorite sample (Y2001); (b) monzogranite sample (Y2002); (c,d) granite sample (Y2046, Y2047); (e,f) syenogranite sample (Y2058, Y2059).

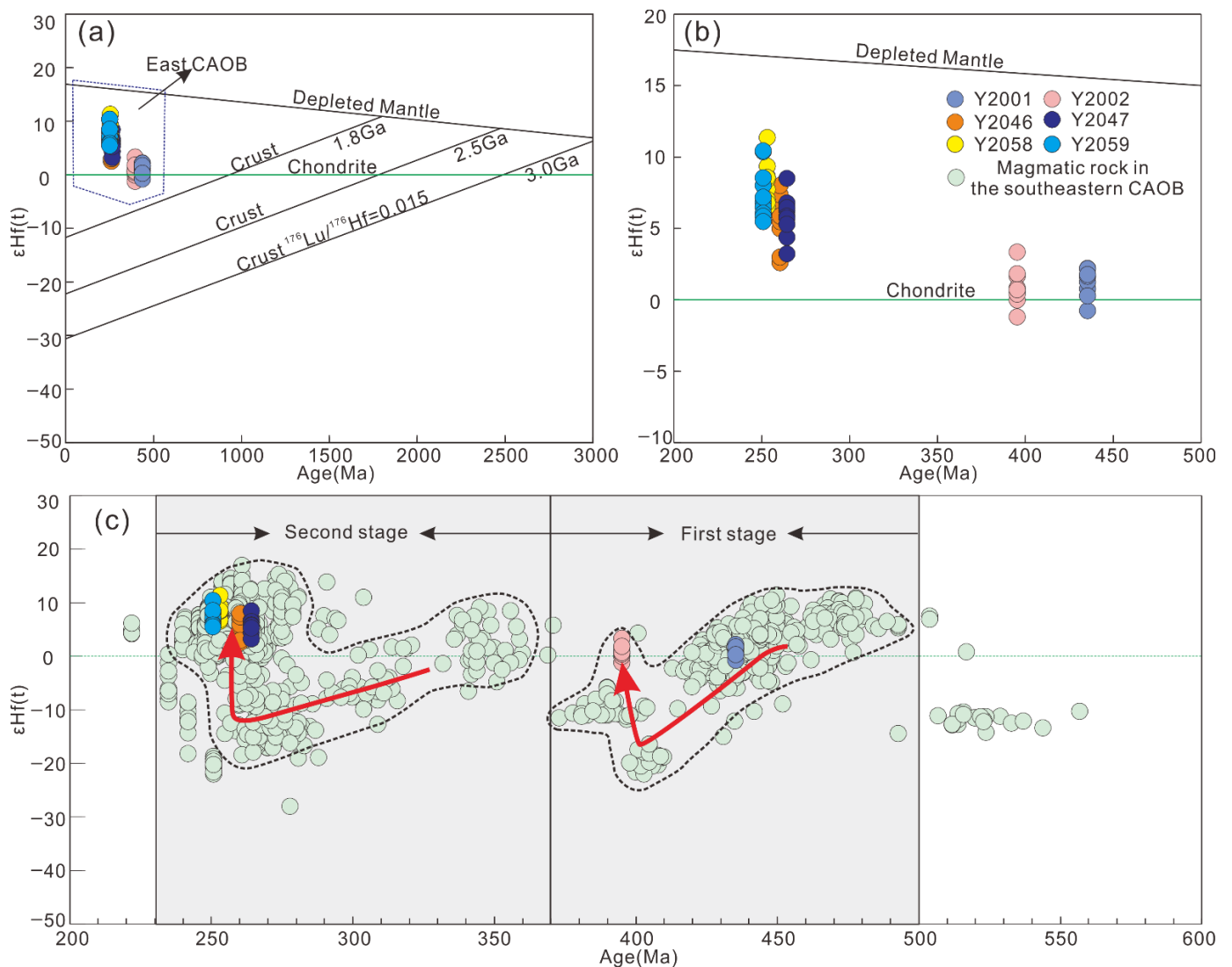


Figure 7. Diagram showing variations of $\epsilon\text{Hf}(t)$ vs. age (Ma) (a–c) for Paleozoic to Triassic magmatic rocks in the southeastern CAOB. Depleted mantle is from Zindler [44]. Hf isotopic data are from [9,12,19,22,23,30,45].

3.2. Major and Trace Element Geochemistry

The geochemical element composition is given in supplementary material Table S4. All samples have low loss on ignition (LOI; 0.33–1.72 wt.%) and their MgO, P₂O₅, TiO₂, MnO contents are less than 1 wt.%. They have medium to high SiO₂ contents (59.28–76.95 wt.%) and Al₂O₃ contents (12.50–17.76 wt.%). The sample Y2001 have high CaO (6.65–7.20 wt.%) and Fe₂O₃^T (6.83–7.06 wt.%), whereas other rocks have high K₂O (3.51–5.73 wt.%) and Na₂O (3.98–5.07 wt.%) contents. According to the QAP diagram (Figure 8), sample Y2001 are quartz diorites, samples Y2002, Y2046 and Y2047 are monzogranites, samples Y2058 and Y2059 are syenogranite.

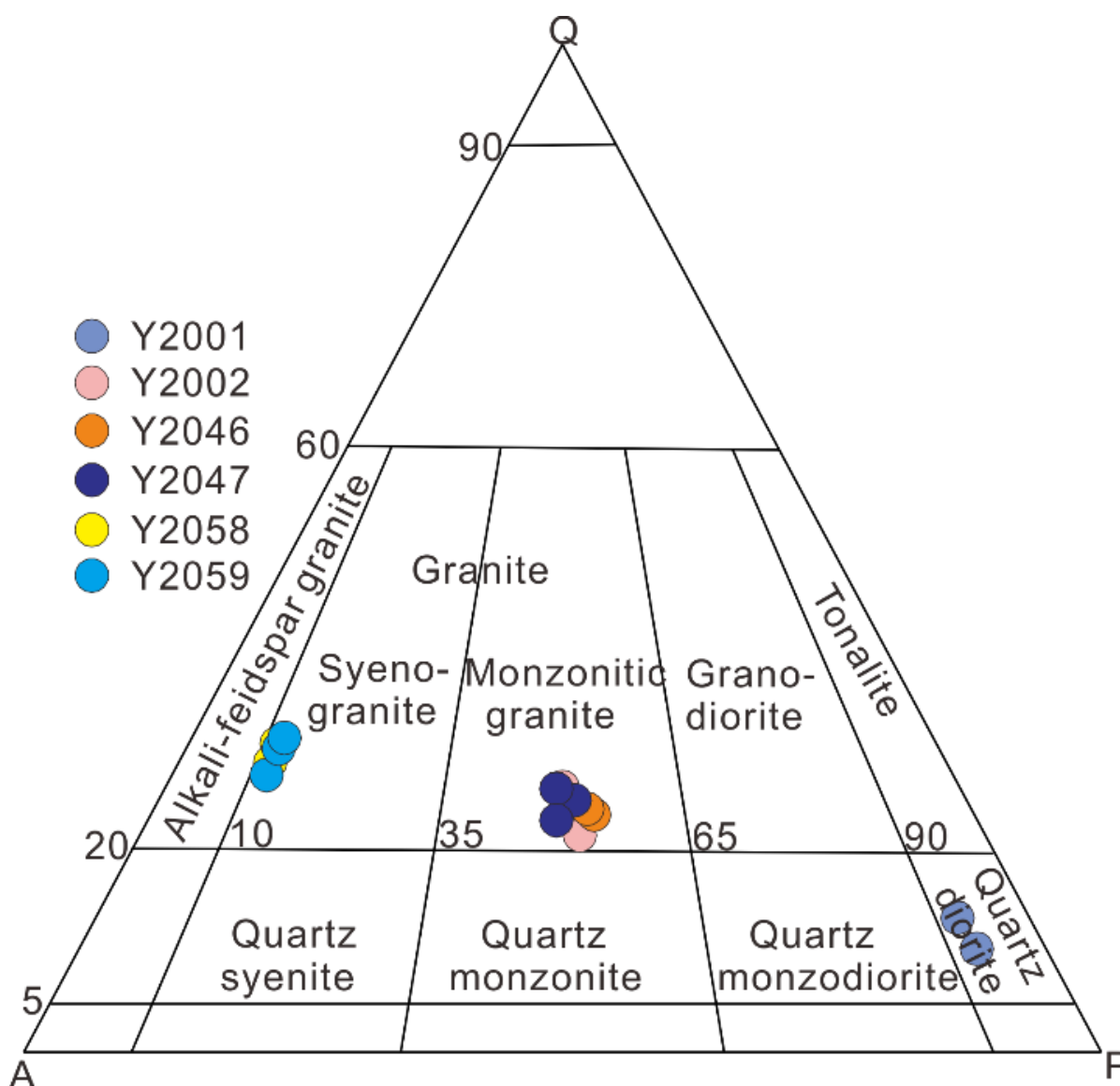


Figure 8. A ternary QAP plot showing the relative modal proportions of quartz (Q), alkali feldspar (A), and plagioclase (P) for the rocks [46,47].

The analyzed samples have low to medium total rare earth element (REE) contents of 22–154 ppm. Granite samples (Y2046 and Y2047) have obvious enrichment in LREE and are depleted in HREE, with high $(La/Yb)_N$ ratios (10.55–15.12), but others show weak to medium enrichment in LREE with lower $(La/Yb)_N$ ratios (1.28–8.16; Figure 9). Syenogranite (Y2058 and Y2059) display distinct negative Eu anomalies ($Eu/Eu^* = 0.08–0.27$), whereas others show no obvious Eu anomalies (0.82–2.32; Figure 9). All of them are enriched in Th, U, K, Pb, Sr, Zr and Hf and depleted in Nb, Ta, La, Ce, P, and Ti (Figure 9).

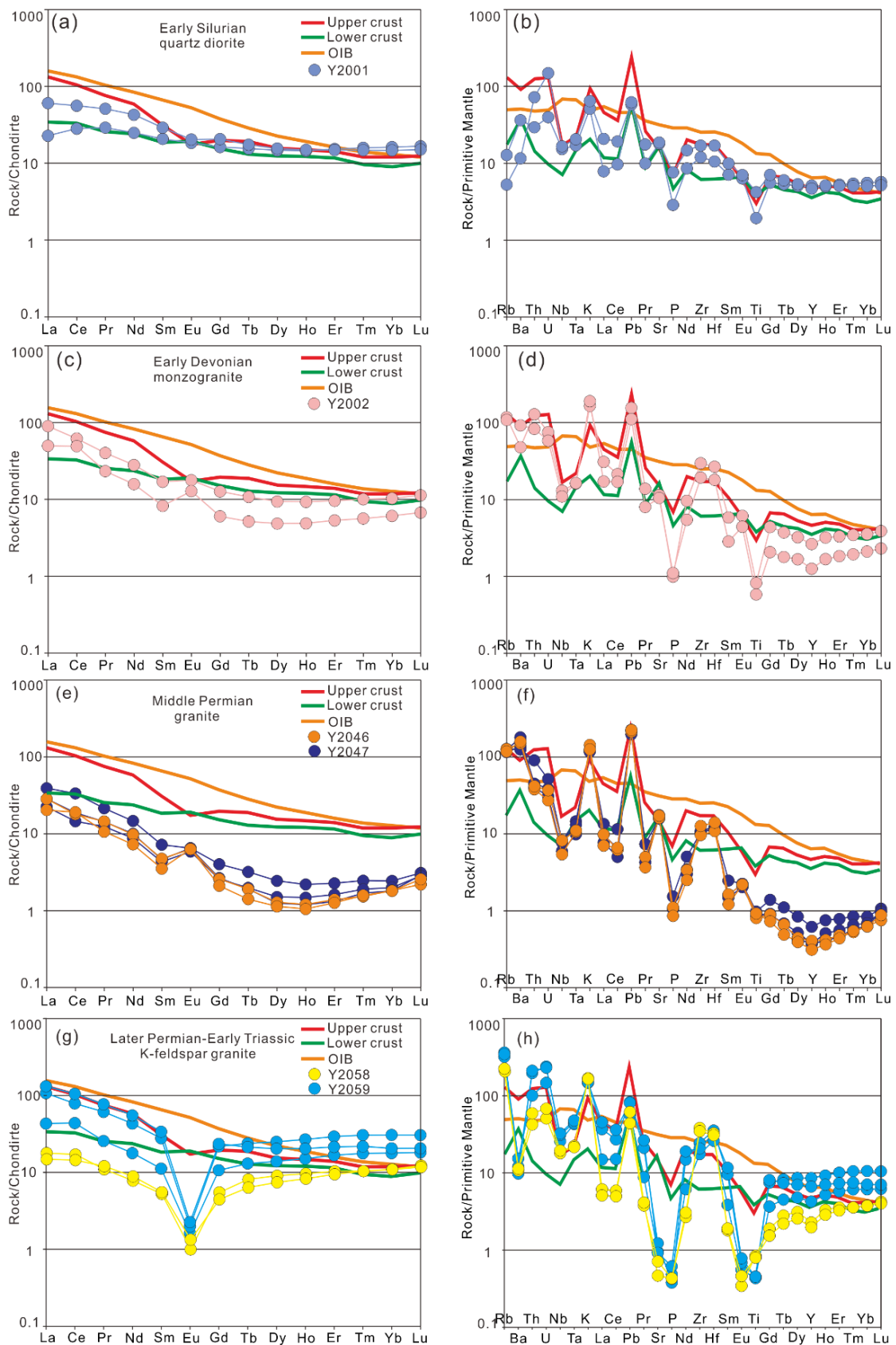


Figure 9. Chondrite-normalized REE patterns (a,c,e,g), and primitive mantle-normalized trace elements diagrams (b,d,f,h) for the analyzed samples [48,49]. Upper and lower continental crust data are from Ref. [50]; OIB data is from Ref. [49].

4. Discussion

4.1. Petrogenesis

4.1.1. Early Silurian Quartz Diorites

The Early Silurian quartz diorites are characterized by intermediate SiO_2 (59.28–61.80 wt.%), low MgO (0.63–0.68 wt.%) with $\text{Mg}^\#$ 17.7–18.4. These features show that the quartz diorites originated from crust-derived sources. Furthermore, they have low mantle-compatible elements, such as Ni (6.14–7.67 ppm) and Co (5.73–7.15 ppm), which suggests that the mantle-derived materials contributed little to their formation [45,51]. Their incompatible element ratios, such as Nb/U (3.79–13.06), and Nb/Ta (14.03–15.59) are also close to continental crust (8.93 and 11, respectively) rather than primitive mantle (30 and 17.5) levels [52,53]. Based on the normalized REE and trace elements patterns, their sources nearly match average lower crust (Figure 9a,b). Zircons from quartz diorites yield mainly low positive $\epsilon\text{Hf}(t)$ values (−0.76 to 2.21; Figure 7), implying that their original magma may have had little input from the mantle. Therefore, we suggest that they originated from partial melting of mafic lower crust.

4.1.2. Early Devonian Monzogranites and Late Permian–Early Triassic Syenogranite

Granites are usually classified into I-type, A-type, S-type, and M-type due to the different source and geochemical characteristics [52,53]. S-type granite usually is strongly peraluminous, whereas the monzogranites and syenogranite lack the aluminous minerals (e.g., cordierite, muscovite) and are weakly peraluminous ($A/\text{CNK} < 1.1$). They also show extremely low P_2O_5 contents (~0.01–0.02 wt.%), which is not consistent with the typical features of S-type granite [54,55]. Monzogranites and syenogranite have high Zr + Nb + Ce + Y elements (260–390 ppm; 261–461 ppm, respectively) and high total alkali contents (9.98–10.80 wt.%; 8.46–9.29 wt.%, respectively), consistent with A-type granite [54,56]. Furthermore, they display high zircon saturation temperatures (807–885 °C; Supplementary Material Table S4) based on Watson and Harrison's [57] formula. In the $\text{Na}_2\text{O} + \text{K}_2\text{O}$ vs $10,000\text{Ga}/\text{Al}$ and Zr vs $10,000\text{Ga}/\text{Al}$ diagrams (Figure 10a,b), they also plot within the region of A-type granite. In conclusion, we believe that the monzogranites and syenogranite belong to A-type granite.

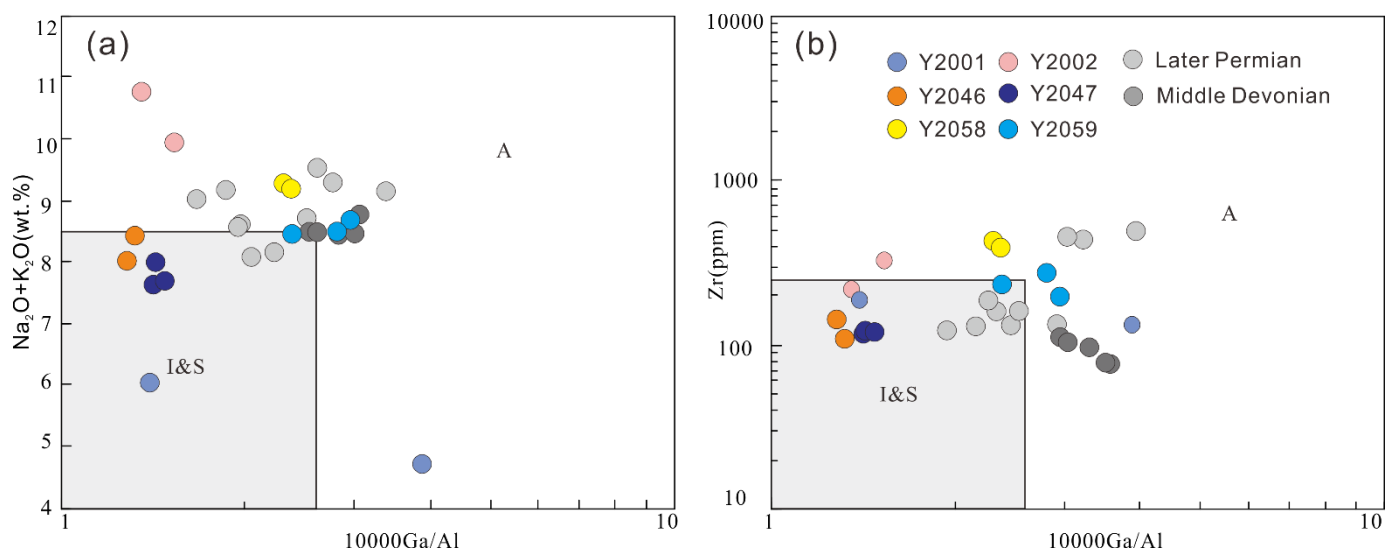


Figure 10. (a) $\text{Na}_2\text{O} + \text{K}_2\text{O}$ vs $10,000 \text{ Ga}/\text{Al}$, and (b) Zr vs $10,000 \text{ Ga}/\text{Al}$ diagrams showing the A-type signature of the analyzed samples [57]. Middle Devonian rocks are from [19]; Late Permian rocks are from [17].

A-type granites are usually formed in the following ways: fractional crystallization of mantle-derived basaltic melt [58,59], or partial melting of crust [60], or crust-mantle mix-

ing [61]. High SiO_2 contents (65.67–76.95 wt.%), low Mg (0.02–0.21 wt.%), $\text{Mg}^\#$ (3.26–16.9) and low mantle-compatible element contents (e.g., Co, 0.41–2.23 ppm; Ni, 2.06–9.22 ppm; Cu, 2.26–9.95 ppm) suggest that these rocks originated from partial melting of crustal material rather than mantle magma. The monzogranites and syenogranite show positive Zr and Hf anomalies, negative Nb, Ta, and Sr anomalies (Figure 9d), which also are typical features of crustal sources. Their Nb/U (4.42–12.04), and Nb/Ta (10.45–15.71) ratios are near to continental crust rather than mantle. Monzogranites have $\epsilon_{\text{Hf}}(t)$ values (between -1.20 and $+3.34$); hence, we believe that they originated from crust modified by mantle-derived source fluids or melts. Syenogranite have high $\epsilon_{\text{Hf}}(t)$ values (5.49–11.36), which suggest that their source might be juvenile crust generated from partial melting of depleted mantle.

4.1.3. Middle Permian Granites

The Middle Permian granites have high Sr (332–370 ppm), high Sr/Y ratios (118–257), low Y (1.42–2.82 ppm) and low Yb (0.31–0.41 ppm), showing characteristic of adakite [62]. In the Sr/Y vs. Y and $(\text{La}/\text{Yb})_N$ vs. Yb_N diagrams (Figure 11a,b) [63,64], the samples plot also within the adakite region. Therefore, we feel that the granites match the composition of adakite. Previous studies show that adakites are mainly formed in the following ways: partial melting of subducted ocean slabs [62,65], delaminated lower crust [66,67], thickened mafic lower crust [68,69] or by fractional crystallization of basaltic magma [70,71].

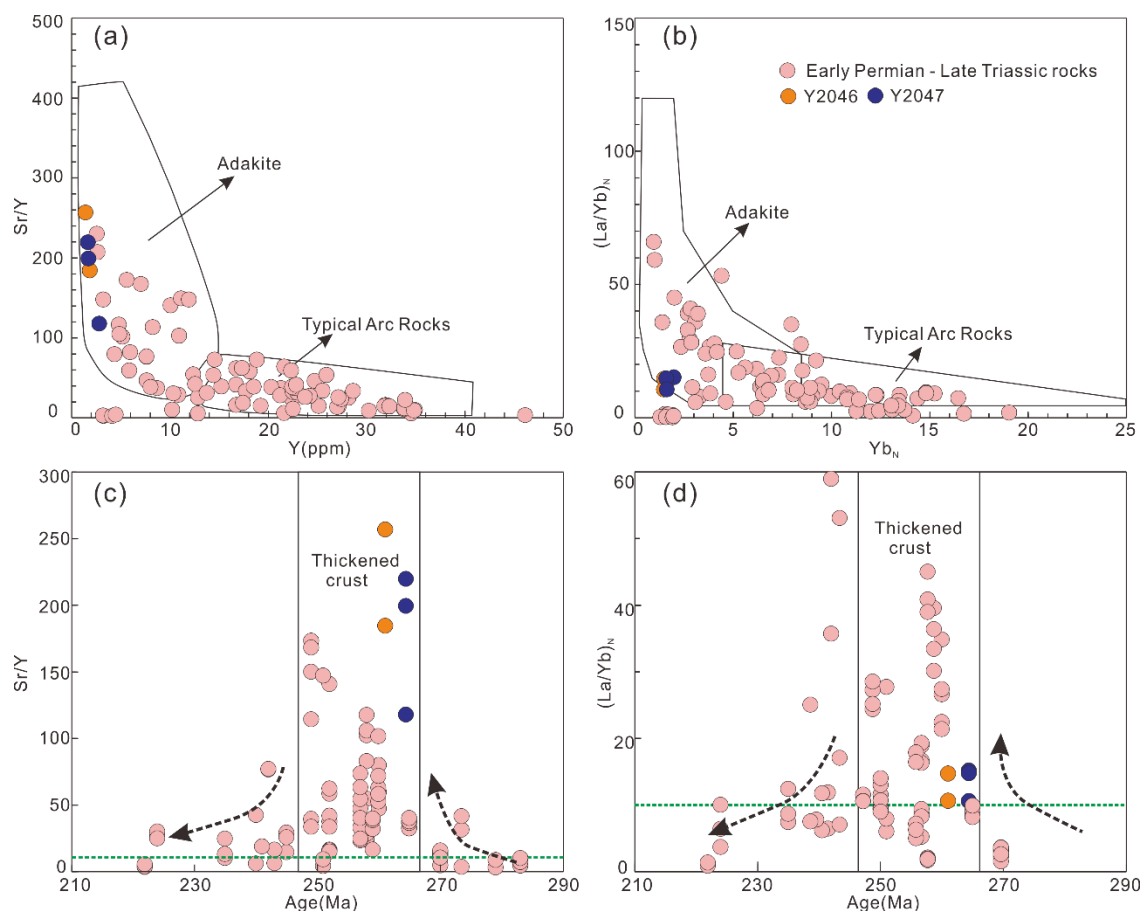


Figure 11. Sr/Y vs. Y (a), $(\text{La}/\text{Yb})_N$ vs. Yb_N (b), Sr/Y vs. Age (c), $(\text{La}/\text{Yb})_N$ vs. Age (d), for the Middle Permian granites (after [63,64]). Data are from [30,35,36].

Partial melting of subducted ocean slabs usually results in low $\text{K}_2\text{O}/\text{Na}_2\text{O}$ ratios (~ 0.5), high MgO (~ 4 – 9 wt.%), and high mantle-compatible elements [62,72]. The melt produced by partial melting of delaminated lower crust will interact with mantle during the upward migration, leading to geochemical characteristics similar to those of partially molten sub-

duction oceanic slabs [73]. The Middle Permian granites have low MgO (0.22–0.26 wt.%), Ni (4.3–14.1 ppm), Co (1.44–3.29 ppm), and high K₂O/Na₂O ratios (0.84–1.05), indicating they were not derived from partial melting of a subducted slab or delaminated lower crust. There are no contemporaneous mafic rocks in the area, indicating that the granites were not derived from the crystallization of basaltic magma. High SiO₂ contents (71.27–72.78 wt.%), low Mg (0.22–0.26 wt.%), Mg[#] (18.1–21.1) and low mantle-compatible element contents (e.g., Co, 1.44–3.29 ppm; Cu, 4.85–12.06 ppm) also suggest that the rocks originated from partial melting of crustal material rather than from fractional crystallization of mantle magma. Rocks from the Late Permian also have high Sr/Y and (La/Yb)_N ratios (Figure 11c,d), which suggests the presence of thickened crust during the Late Permian. In addition, the high εHf(t) isotopic values (2.99–8.50) of these granites also suggest that their source was juvenile thickened lower crust.

4.2. Tectonic Evolution and Implications

4.2.1. Tectonic Evolution

The eastern PAO in the southeastern CAOB has a complex evolution history during the Paleozoic to Triassic [13,14,74]. Previous studies show that the magmatic rocks in the southeastern CAOB can be assigned to two periods: (1) Late Cambrian to Early Devonian [12,13,19]; (2) Early Permian to Triassic [14,18]. Although some valuable conclusions have been reached by the study of these rocks, for example, the agreement that the Solonker-Xar Moron-Changchun suture zone is the final closure location of the eastern PAO [14,18], there are still some controversial issues. The biggest controversy is the timing of the final closure of the eastern PAO. There are mainly two suggestions: (1) Devonian-Carboniferous [19,28–31]; (2) Late Permian to Middle Triassic [18,22,23].

The Silurian quartz diorites show typical island arc features and resemble the medium-K calc-alkaline series; they are enriched in large ion lithophile elements (LILE, e.g., Th and U), depleted in high field strength elements (HFSE, e.g., Nb, Ta and Ti) (Figure 9b). In the tectonic discrimination diagram Rb vs. Y + Nb (Figure 12a,b), these quartz diorites fall into the volcanic arc area. Previous studies have shown that the Silurian rocks are mainly intermediate in SiO₂ and medium to high in K₂O with typical island arc features (Supplementary Material Figure S2a,b). Hence, we consider that Early Silurian quartz diorites were formed in a subduction setting. During the Late Silurian, angular unconformable of the strata (Xuniwusu Fm and Xibiehe Fm) were observed. We suggest that the Late Silurian is a period of tectonic transformation. The tectonic setting changes from subduction to closure. The Early Devonian monzogranites are A type granites. The Devonian rocks are mainly granitic high-K rocks (Supplementary Material Figure S2b), and have some Devonian A-type granites [19], which suggests that the southeastern CAOB was an extensional tectonic setting during the Devonian.

The eastern PAO experienced subduction-collision-extension from Silurian to Devonian, so does it represents the final closure of the eastern PAO? Studies also show that there is an abundance of subduction-related magmatic rocks in the Permian-Triassic (Figures 2 and 13) [30,32]. The Paleo-Pacific Ocean in NE China opened after the Triassic [75]. Hence, these Permian magmatic rocks are not associated with Paleo-Pacific Ocean and so they must have formed during the evolution of the eastern PAO [22,23,76]. This indicates that the final closure time is not at the Devonian.

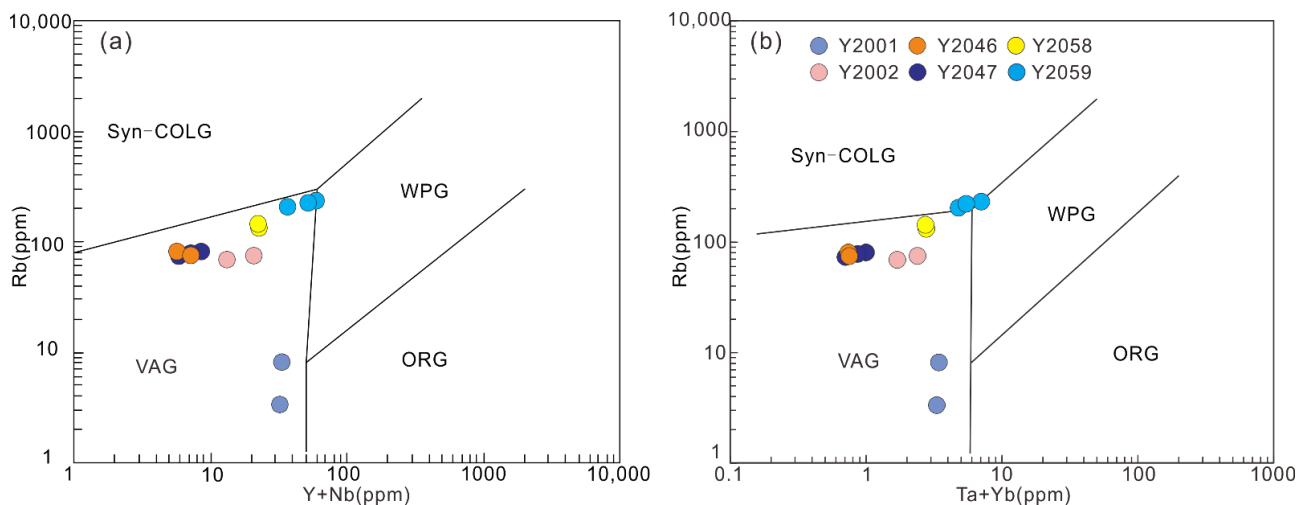


Figure 12. Tectonic discrimination diagrams of (Y + Nb)-Rb (a); (Ta + Yb)-Rb (b) for the analyzed samples (after [74]). Syn-COLG: syn-collision granites; ORG: Ocean ridge granites; VAG: volcanic arc granites; WPG: within-plate granites. The data source is the same as for Figure 7.

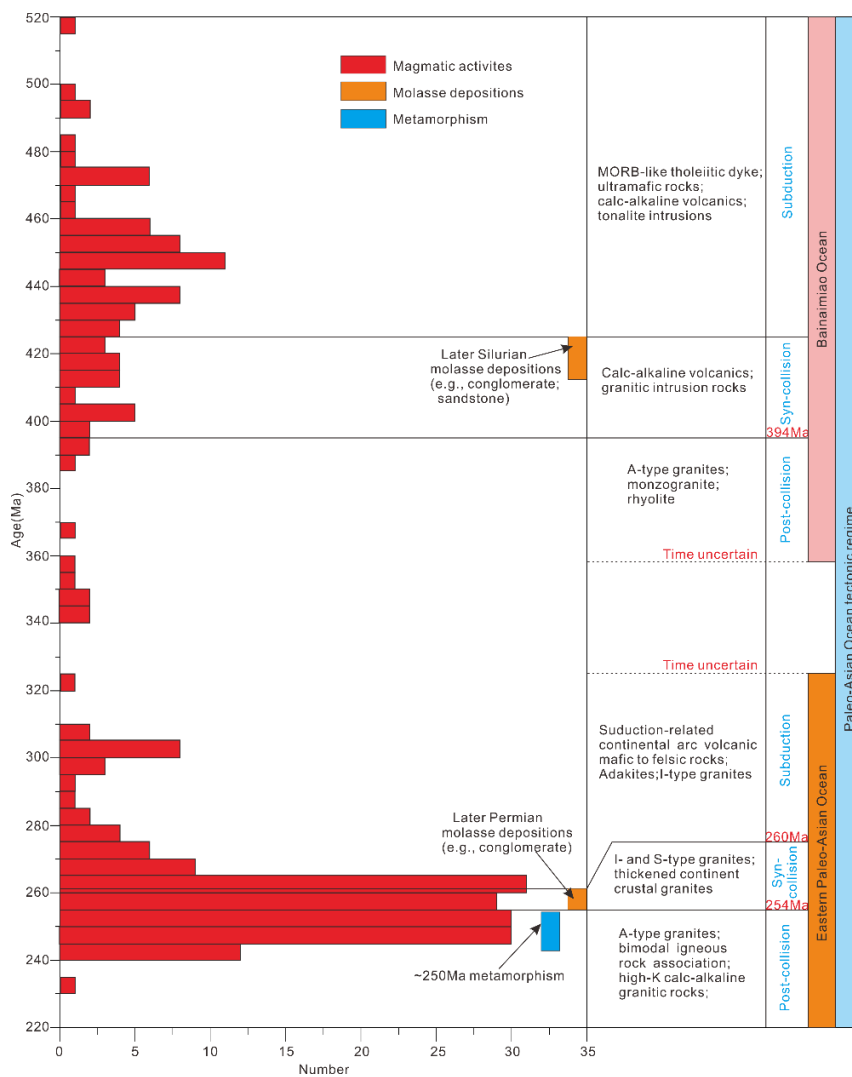


Figure 13. Histogram of zircon U-Pb ages from Paleozoic to Triassic magmatism in the southeastern CAOB. Ages (in Ma); references are listed in Supplementary Table S1.

The Middle Permian adakites (264.4–260.5 Ma) in this study were formed by partial melting of a juvenile thickened lower crust. Adakitic rocks are emplaced at the beginning of a subduction zone. Previous studies show that the Early-Middle Permian rocks are mainly medium-high K calc-alkaline and subalkaline rocks in an active continental margin setting (Supplementary Material Figure S3a,b) [30,45,77], indicating southward subduction of the eastern PAO beneath the northern margin of the NCC during Early-Middle Permian. Molasse deposits formed during the in Late Permian [76,78]. The Hulan Group has a deposition age of 287 Ma and a metamorphic age of 250 Ma in the central Jilin Province [79]. This evidence suggests that the eastern PAO was in a collision stage in the Late Permian. During the Late Permian-Early Triassic, many medium-high K magmatic rocks were formed (Supplementary Material Figure S3a,b), as well as some A-type granites and bimodal igneous assemblages (Figure 10) [17,30,76,80]. Hence, considering the age of the A-type granites in this paper, we believe that the eastern PAO entered the post-collision extension stage at ~254 Ma, which represents the final closure time of the eastern PAO. After the Late Triassic, NE China entered the formation of the Pacific Ocean [75].

4.2.2. Tectonic Implications

The above discussion leads to an important question: why are there two stages of subduction-collision-extension of the eastern PAO from the Paleozoic to the Triassic? According to the differences between the Bainaimiao arc and the NCC in the early Paleozoic sedimentary metamorphic rocks and volcanic rocks, the Bainaimiao arc belt is considered to be an accretionary island arc that divides the ancient Asian ocean into two parts (i.e., PAO and Bainaimiao ocean; Figure 14a) [12,81,82]. The first stage is the evolution of the Bainaimiao ocean from Late Cambrian to Early Devonian (Figures 13 and 14a–c). In fact, there is also some evidence supporting the existence of the Bainaimiao ocean. For example, ophiolites (Figure 1b) along the Bayan Obo–Chifeng–Kaiyuan fault zone, recognized in Wude north to the Bayan Obo and Bainaimiao area (Figure 1b) [13,83,84], could represent the suture zone of an arc-continent collision. Secondly, the Bainaimiao and Damaoqi regions have a large area where flysch, volcanic rock, and carbonate formations occur, typical of an ocean basin, formed in the Early Silurian (441–438 Ma) [85,86]. The Early Paleozoic volcanic arc rocks distributed on the Bainaimiao arc also support the existence of the ocean basin (Figure 1b) [12,13]. Due to the Ondor Sum subduction complex in the north of the Bainaimiao arc having the features of the top-to-the-NW sense of shear and high P/T facies rocks, the subduction polarity of the Bainaimiao ocean is northward (Figure 1b) [82]. As subduction continued, the Bainaimiao ocean closed in the Late Silurian, forming the molasse deposits and angular unconformity between Xuniwusu and Xiebiehe Fm [21]. The Bainaimiao arc accretion to North China Cratons could suggest that the arc-continent collision had an important role in the formation of the CAOB. During the Early Devonian, the northern margin of the NCC was in an orogenic extension setting, possibly due to the subducted slab break-off of the Bainaimiao ocean (Figure 14c), resulting in the formation of some A-type granites (e.g., in this study). The second stage is the final closure of the eastern PAO from Early Permian to Triassic (Figures 13 and 14d–f). The eastern PAO experienced double-sided subduction in the Early-Middle Permian that is supported by occurrence of adakites and high-Mg diorites on both sides [87,88]. The eastern PAO was in the collision stage in the Late Permian, and entered the extension stage at ~254 Ma (Figure 14e,f). Hence, the evolution of the eastern PAO can be divided into two orogenic cycles (Figures 13 and 14).

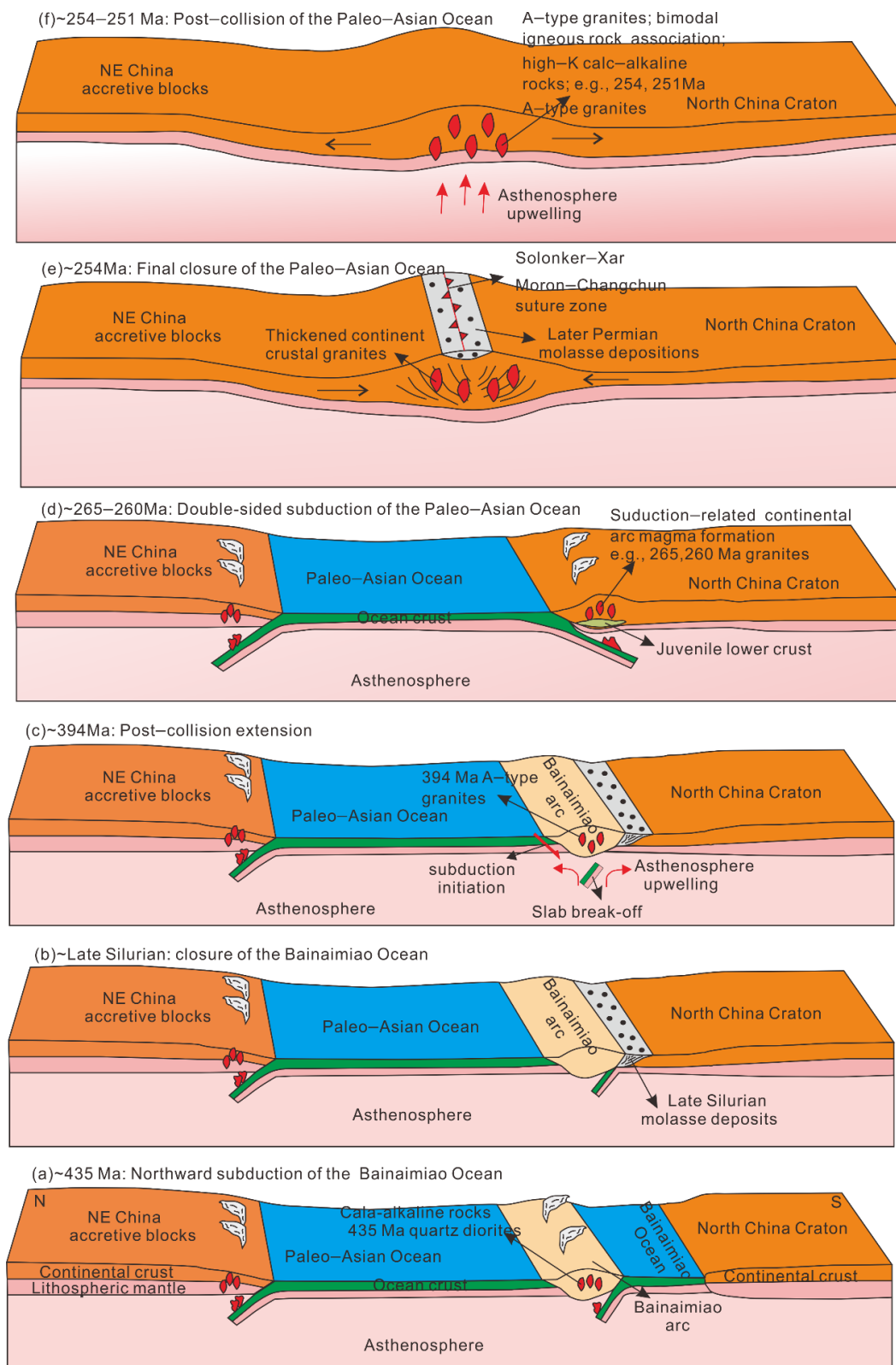


Figure 14. Schematic diagram of the eastern PAO from Paleozoic to Early Triassic in the southeastern CAOB. (a) northward subduction of the Bainaimiao ocean; (b) closure of the Bainaimiao ocean; (c) post-collision extension of the Bainaimiao ocean; (d) double-sided subduction of the Paleo-Asian Ocean; (e) final closure of the Paleo-Asian Ocean; (f) post-collision extension of the Paleo-Asian Ocean.

We observe some time variation of Hf isotopes ($\epsilon\text{Hf}(t)$), which corresponds to the two-stage evolution of the eastern PAO (Figure 7c). Hf isotope values decrease slowly during subduction. This may be due to the thickening of the crust caused by subduction. During this stage, the melts produced from a mantle source cannot easily rise through the crust due to their relatively high density. Lower-density melts formed by remelting within the crust are more likely to be emplaced at shallow levels; hence, Hf isotopes will be relatively low. During the extensional stage, Hf isotope values vary widely. Possibly the asthenosphere rose and heated the crust, producing large amounts of melt. Under extensional conditions, mantle-derived rocks with high Hf isotopic compositions value are more likely to be uplifted and emplaced at shallow levels. The diversity of magmatic sources leads to a wide range of Hf isotope values. Hence, Hf isotope values also support the two-stage orogenic cycle of the eastern PAO, consistent with our proposed model.

5. Conclusions

- (1) We have identified four periods of magmatism in the southeastern Central Asian Orogenic Belt, namely Early Silurian quartz diorites (434.7 Ma), Early Devonian monzogranites (394.2 Ma), Middle Permian granites (260.2–264.5 Ma) and Late Permian–Early Triassic syenogranite (250.8–253.6 Ma).
- (2) The quartz diorites originated from partial melting of mafic lower crust with minor, if any, mantle contribution. The monzogranites were derived from the crust modified by mantle-derived fluids or melts. The granites are adakitic in composition and originated from juvenile thickened lower crust. The syenogranites were derived from juvenile crust that formed by partial melting of depleted mantle. The quartz diorites and granites were formed in a subduction setting, and the monzogranites and syenogranite were formed in an extensional setting.
- (3) The subduction of the eastern PAO can be divided into two stages. The first stage is the evolution of the Bainaimiao ocean from the Late Cambrian to the Early Devonian and the second stage is the final closure evolution from the Early Permian to the Triassic. The final closure time is Late Permian (~254 Ma).

Supplementary Materials: The following supporting information can be downloaded at: <https://www.mdpi.com/article/10.3390/min12081040/s1>, Figure S1: Tectonic map of China; Figure S2: Geochemistry of the Cambrian to Devonian rocks of central Jilin Province in the southeastern CAOB. (a) Total alkali vs SiO_2 (TAS) diagrams; (b) SiO_2 vs K_2O diagrams. Tectonic discrimination diagrams of (Y + Nb)-Rb (c); (Ta + Yb)-Rb (d) for the Cambrian to Devonian rocks in the central Jilin Province; Figure S3: Geochemistry of the Early Permian to Late Triassic rocks of central Jilin Province in the southeastern CAOB. (a) Total alkali vs SiO_2 (TAS) diagrams; (b) SiO_2 vs K_2O diagrams. Tectonic discrimination diagrams of (Y + Nb)-Rb (c); (Ta + Yb)-Rb (d) for the Early Permian to Late Triassic rocks in the central Jilin Province; Table S1: Zircon age data for the Paleozoic-Triassic magmatic rocks in the southeastern CAOB; Table S2: LA-ICP-MS zircon U-Pb dating data for the samples; Table S3: Zircon Hf isotope results for the samples; Table S4: Major (wt.%) and trace element (ppm) compositions for the samples.

Author Contributions: Writing—original draft preparation, J.S.; writing—review and editing, J.S., Y.Q., Y.S. and F.S.; formal analysis, J.L. and L.Z.; investigation, J.S., J.L. and Y.Q.; funding acquisition, Y.Q. All authors have read and agreed to the published version of the manuscript.

Funding: This research was funded by the Natural Science Foundation of Jilin Province [Grant No. 20220101161JC], Natural Science Foundation of China [Grant No. 41402060], Self-determined Foundation of Key Laboratory of Mineral Resources Evaluation in Northeast Asia, Ministry of Natural Resources [Grant No. DBY-ZZ-19-13, BY-ZZ-19-15].

Institutional Review Board Statement: Not applicable.

Informed Consent Statement: Not applicable.

Data Availability Statement: Not applicable.

Acknowledgments: We thank Jovana Nikolic, and two anonymous referees for comments which helped in improving our manuscript.

Conflicts of Interest: The authors declare no conflict of interest.

References

1. Wilson, J.T. Did the Atlantic close and then re-open? *Nature* **1966**, *211*, 676–681. [[CrossRef](#)]
2. Li, S.Z.; Yang, Z.; Zhao, S.J.; Li, X.Y.; Guo, L.L.; Yu, S.; Liu, X.; Suo, Y.H.; Li, H.Y. Global Early Paleozoic Orogens (I): Collision-Type Orogeny. *J. Jilin Univ. (Earth Sci. Ed.)* **2016**, *46*, 945–967. (In Chinese with English Abstract)
3. Li, S.Z.; Yang, Z.; Zhao, S.J.; Li, X.Y.; Suo, Y.H.; Guo, L.L.; Yu, S.; Dai, L.M.; Li, S.J.; Mou, D.L. Global Early Paleozoic Orogens (II): Subduction-Accretionary-Type Orogen. *J. Jilin Univ. (Earth Sci. Ed.)* **2016**, *46*, 968–1004. (In Chinese with English Abstract)
4. Li, S.Z.; Li, X.Y.; Zhao, S.J.; Yang, Z.; Liu, X.; Guo, L.L.; Wang, Y.M.; Hao, Y.; Zhang, J.; Hu, M.Y. Global Early Paleozoic Orogens (III): Intracontinental Orogen in South China. *J. Jilin Univ. (Earth Sci. Ed.)* **2016**, *46*, 1005–1025. (In Chinese with English Abstract)
5. Cawood, P.A.; Kröner, A.; Collins, W.J.; Kusky, T.M.; Mooney, W.D.; Windley, B.F. Accretionary orogens through Earth history. *Geol. Soc. Spec. Publ.* **2009**, *318*, 11–36. [[CrossRef](#)]
6. Groves, D.L.; Bierlein, F.P. Geodynamic settings of mineral deposit systems. *J. Geol. Soc. Lond.* **2007**, *164*, 19–30. [[CrossRef](#)]
7. Sengör, A.M.C.; Natal'in, B.A.; Burtman, V.S. Evolution of the Altaid tectonic collage and Palaeozoic crustal growth in Eurasia. *Nature* **1993**, *364*, 299–307. [[CrossRef](#)]
8. Xiao, W.; Windley, B.F.; Han, C.; Liu, W.; Wan, B.; Zhang, J.; Ao, S.; Zhang, Z.; Song, D. Late Paleozoic to early Triassic multiple roll-back and oroclinal bending of the Mongolia collage in Central Asia. *Earth Sci. Rev.* **2017**, *186*, 94–128. [[CrossRef](#)]
9. Zhou, J.B.; Cao, J.L.; Wilde, S.A.; Zhao, G.C.; Zhang, J.J.; Wang, B. Paleo-Pacific subduction-accretion: Evidence from Geochemical and U-Pb zircon dating of the Nadanhada accretionary complex, NE China. *Tectonics* **2014**, *33*, 2444–2466. [[CrossRef](#)]
10. Wu, F.Y.; Sun, D.Y.; Ge, W.C.; Zhang, Y.B.; Grant, M.L.; Wilde, S.A.; Jahn, B.M. Geochronology of the Phanerozoic granitoids in northeastern China. *J. Asian Earth Sci.* **2011**, *41*, 1–30. [[CrossRef](#)]
11. Khain, E.V.; Bibikova, E.V.; Salnikova, E.B.; Kröner, A.; Gibsher, A.S.; Didenko, A.N.; Degtyarev, K.E.; Fedotova, A.A. The Pale-Asian Ocean in the Neoproterozoic and early Paleozoic: New geochronologic data and Paleotectonic reconstructions. *Precambrian Res.* **2003**, *122*, 329–358. [[CrossRef](#)]
12. Zhang, S.H.; Zhao, Y.; Ye, H.; Liu, J.M.; Hu, Z.C. Origin, and evolution of the Bainaimiao arc belt: Implications for crustal growth in the southern Central Asian orogenic belt. *Bull. Geol. Soc. Am.* **2014**, *126*, 1275–1300. [[CrossRef](#)]
13. Jian, P.; Liu, D.; Kröner, A.; Windley, B.F.; Shi, Y.; Zhang, F.; Shi, G.; Miao, L.; Zhang, W.; Zhang, Q.; et al. Time scale of an early to mid-Paleozoic orogenic cycle of the long-lived Central Asian Orogenic Belt, Inner Mongolia of China: Implications for continental growth. *Lithos* **2008**, *101*, 233–259. [[CrossRef](#)]
14. Xiao, W.; Windley, B.F.; Hao, J.; Zhai, M. Accretion leading to collision and the Permian Solonker suture, Inner Mongolia, China: Termination of the central Asian orogenic belt. *Tectonics* **2003**, *22*, 1484–1505. [[CrossRef](#)]
15. Han, Y.G.; Zhao, G.; Cawood, P.A.; Sun, M.; Eizenhöfer, P.R.; Hou, W.; Zhang, X.; Liu, Q. Tarim and North China cratons linked to northern Gondwana through switching accretionary tectonics and collisional orogenesis. *Geology* **2016**, *44*, 95–98. [[CrossRef](#)]
16. Han, Y.G.; Zhao, G.; Sun, M.; Eizenhöfer, P.R.; Hou, W.; Zhang, X.; Liu, Q.; Wang, B.; Liu, D.; Xu, B. Late Paleozoic subduction, and collision processes during the amalgamation of the Central Asian Orogenic Belt along the South Tianshan suture zone. *Lithos* **2016**, *246–247*, 1–12. [[CrossRef](#)]
17. The Paleozoic Tectonic Evolution of The west Segment of the Northern Margin of the North China Craton: Implication from the Magmatic Evidence of Damao Region. Ph.D. Thesis, Northwest University, Xi'an, China, 2019. (In Chinese).
18. Liu, C.; Zhao, G.; Liu, F.; Shi, J. Detrital zircon U-Pb and Hf isotopic and whole-rock geochemical study of the Bayan Obo Group, northern margin of the North China Craton: Implications for Rodinia reconstruction. *Precambrian Res.* **2017**, *303*, 372–391. [[CrossRef](#)]
19. Shi, Y.; Liu, D.; Miao, L.; Zhang, F.; Jian, P.; Zhang, W.; Hou, K.; Xu, J. Devonian A-type granitic magmatism on the northern margin of the North China Craton: SHRIMP U-Pb zircon dating and Hf-isotopes of the Hongshan granite at Chifeng, Inner Mongolia, China. *Gondwana Res.* **2010**, *17*, 632–641. [[CrossRef](#)]
20. Xu, B.; Charvet, J.; Chen, Y.; Zhao, P.; Shi, G. Middle Paleozoic convergent orogenic belts in western Inner Mongolia (China): Framework, kinematics, geochronology, and implications for tectonic evolution of the Central Asian Orogenic Belt. *Gondwana Res.* **2013**, *23*, 1342–1364. [[CrossRef](#)]
21. Zhang, Y.P.; Su, Y.Z.; Li, J.C. Regional tectonics significance of the Late Silurian Xibiehe Formation in central Inner Mongolia, China. *Geol. Bull. China* **2010**, *29*, 1599–1605. (In Chinese)
22. Jing, Y.; Ge, W.; Dong, Y.; Yang, H.; Ji, Z.; Bi, J.; Zhou, H.; Xing, D. Early Middle Permian southward subduction of the eastern Paleo-Asian Ocean: Constraints from geochronology and geochemistry of intermediate-acidic volcanic rocks in the northern margin of the North China Craton. *Lithos* **2020**, *364–365*, 10549. [[CrossRef](#)]
23. Jing, Y.; Ji, Z.; Ge, W.C.; Dong, Y.; Yang, H.; Bi, J.H. Middle-late Permian I-type granitoids from the Diaobingshan region in the northern margin of the North China Craton: Insight into southward subduction of the Paleo-Asian Ocean. *Int. Geol. Rev.* **2020**, *63*, 357–379. [[CrossRef](#)]

24. Jing, Y.; Yang, H.; Ge, W.; Dong, Y.; Ji, Z.; Bi, J.; Zhou, H.; Xing, D. When did the final closure occur of the eastern Paleo-Asian Ocean: Constraints from the latest Early–Middle Triassic adakitic granites in the southeastern Central Asian Orogenic Belt? *Gondwana Res.* **2022**, *103*, 146–171. [[CrossRef](#)]
25. Chen, H.C.; Zhao, G.; Jahn, B.M.; Zhou, H.; Sun, M. Geochemistry, and geochronology of the Delinggou intrusion: Implications for the subduction of the paleo-Asian ocean beneath the north China craton. *Gondwana Res.* **2017**, *43*, 178–192. [[CrossRef](#)]
26. Ge, W.C.; Wu, F.Y.; Zhou, C.Y.; Abdel Rahman, A.A. Emplacement age of the Tahe granite and its constraints on the tectonic nature of the Erguna block in the northern part of the Da Xing’an Range. *Chin. Sci. Bull.* **2005**, *50*, 2097–2105. [[CrossRef](#)]
27. Ge, W.C.; Wu, F.Y.; Zhou, C.Y.; Zhang, J.H. Porphyry Cu–Mo deposits in the Eastern Xing’an–Mongolian orogenic belt: Mineralization ages and their geodynamic implications. *Chin. Sci. Bull.* **2007**, *52*, 3416–3427. [[CrossRef](#)]
28. Zhao, P.; Appel, E.; Xu, B.; Sukhbaatar, T. First Paleomagnetic Result from the Early Permian Volcanic Rocks in Northeastern Mongolia: Evolutional Implication for the Paleo-Asian Ocean and the Mongol-Okhotsk Ocean. *J. Geophys. Res. Solid Earth* **2020**, *125*, e2019JB017338. [[CrossRef](#)]
29. Zhao, P.; Chen, Y.; Xu, B.; Faure, M.; Shi, G.; Choulet, F. Did the Paleo-Asian Ocean between North China Block and Mongolia Block exist during the late Paleozoic? First paleomagnetic evidence from central-eastern Inner Mongolia, China. *J. Geophys. Res. Solid Earth* **2013**, *118*, 1873–1894. [[CrossRef](#)]
30. Cao, H.H.; Xu, W.L.; Pei, F.P.; Wang, Z.W.; Wang, F.; Wang, Z.J. Zircon u–pb geochronology and petrogenesis of the late Paleozoic–early Mesozoic intrusive rocks in the eastern segment of the northern margin of the north China block. *Lithos* **2013**, *170–171*, 191–207. [[CrossRef](#)]
31. Pei, F.P.; Zhang, Y.; Wang, Z.W.; Cao, H.H.; Xu, W.L.; Wang, Z.J.; Wang, F.; Yang, C. Early–Middle Paleozoic subduction–collision history of the south-eastern Central Asian Orogenic Belt: Evidence from igneous and metasedimentary rocks of central Jilin Province, NE China. *Lithos* **2016**, *261*, 164–180. [[CrossRef](#)]
32. Gu, C.; Zhu, G.; Li, Y.; Su, N.; Xiao, S.; Zhang, S.; Liu, C. Timing of deformation and location of the eastern Liaoyuan Terrane, NE China: Constraints on the final closure time of the Paleo-Asian Ocean. *Gondwana Res.* **2018**, *60*, 194–212. [[CrossRef](#)]
33. Zheng, C.Z. New partition of Devonian strata in Jilin Province. *J. Stratigr.* **1989**, *13*, 47–51. (In Chinese)
34. Guo, W.X.; Yin, C.J.; Wang, Y.S. *Description of Geological Map of Changchun City*; Jilin Geological Survey Institute: Changchun, China, 2001. (In Chinese)
35. Wang, Z.J.; Xu, W.L.; Pei, F.P.; Wang, Z.W.; Li, Y. Geochronology, and provenance of detrital zircons from late Paleozoic strata of central Jilin Province, Northeast China: Implications for the tectonic evolution of the eastern Central Asian Orogenic Belt. *Int. Geol. Rev.* **2015**, *25*, 211–228. [[CrossRef](#)]
36. Wang, Z.J.; Xu, W.L.; Pei, F.P.; Wang, Z.W.; Li, Y.; Cao, H.H. Geochronology, and geochemistry of middle Permian–Middle Triassic intrusive rocks from central-eastern Jilin Province, NE China: Constraints on the tectonic evolution of the eastern segment of the Paleo-Asian Ocean. *Lithos* **2015**, *238*, 23–25. [[CrossRef](#)]
37. Chen, Y.J.; Peng, Y.J.; Liu, Y.W.; Sun, G. Dismemberment of Bailazi Formation of the Qinghezhen Group. *J. Jilin Univ. (Earth Sci. Ed.)* **2006**, *36*, 24–31. (In Chinese with English Abstract)
38. Liu, Y.S.; Hu, Z.C.; Gao, S.; Günther, D.; Xu, J.; Gao, C.G.; Chen, H.H. In situ analysis of major and trace elements of anhydrous minerals by LA-ICP-MS without applying an internal standard. *Chem. Geol.* **2008**, *257*, 34–43. [[CrossRef](#)]
39. Ludwig, K.R. *User’s Manual for Isoplot 3.00, a Geochronological Toolkit for Microsoft Excel*; Berkeley Geochronology Center: Berkeley, CA, USA, 2003; no.4. Components.
40. Anderson, T. Correction of common lead in U–Pb analyses that do not report ²⁰⁴Pb. *Chem. Geol.* **2002**, *192*, 59–79. [[CrossRef](#)]
41. Wu, F.Y.; Yang, Y.H.; Xie, L.W.; Yang, J.H.; Xu, P. Hf isotopic compositions of the standard zircons and baddeleyites used in U–Pb geochronology. *Chem. Geol.* **2006**, *234*, 105–126. [[CrossRef](#)]
42. Guo, C.; Chen, Y.; Zeng, Z.; Lou, F. Petrogenesis of the Xihuashan granites in southeastern China: Constraints from geochemistry and in-situ analyses of zircon U–Pb–Hf–O isotopes. *Lithos* **2012**, *148*, 209–227. [[CrossRef](#)]
43. Hoskin, P.W.O.; Schaltegger, U. The composition of zircon and igneous and metamorphic petrogenesis. *Rev. Mineral. Geochem.* **2003**, *53*, 27–62. [[CrossRef](#)]
44. Zindler, A. Chemical Geodynamics. *Annu. Rev. Earth Planet. Sci.* **1986**, *14*, 493–571. [[CrossRef](#)]
45. Cao, H.H.; Xu, W.L.; Pei, F.P.; Guo, P.Y.; Wang, F. Permian tectonic evolution of the eastern section of the northern margin of the North China Plate: Constraints from zircon U–Pb geochronology and geochemistry of the volcanic rocks. *Acta Petrol. Sin.* **2012**, *28*, 2733–2750. (In Chinese with English Abstract)
46. Le Maitre, R.W. *Igneous rocks—A classification and glossary of terms. Recommendations of the IUGS Subcommittee on the Systematics of Igneous Rocks*, 2nd ed.; Cambridge University Press: Cambridge, UK, 2002.
47. Wu, D.Q.; Sun, F.Y.; Pan, Z.C.; Tian, N. Geochronology, Geochemistry, and Hf Isotopic Compositions of Triassic Igneous Rocks in the Easternmost Segment of the East Kunlun Orogenic Belt, NW China: Implications for Magmatism and Tectonic Evolution. *Int. Geol. Rev.* **2020**, *63*, 1011–1029. [[CrossRef](#)]
48. Boynton, W.V. Geochemistry of the rare earth elements: Meteorite studies. In *Rare Earth Element Geochemistry*; Henderson, P., Ed.; Elsevier: Amsterdam, The Netherlands, 1984; pp. 63–114.
49. Sun, S.S.; McDonough, W.F. Chemical, and isotopic systematics of oceanic basalts: Implications for mantle composition and processes. *Geol. Soc. Spec. Publ.* **1989**, *42*, 313–345. [[CrossRef](#)]

50. Rudnick, R.L.; Gao, S. Composition of the Continental Crust. In *Treatise on Geochemistry*, 2nd ed.; Elsevier Science: Amsterdam, The Netherlands, 2003. [[CrossRef](#)]
51. Frey, F.A.; Prinz, M. Ultramafic inclusions from San Carlos, Arizona: Petrologic and geochemical data bearing on their petrogenesis. *Earth Planet. Sci. Lett.* **1978**, *38*, 129–176. [[CrossRef](#)]
52. Taylor, S.R.; McLennan, S.M. The continental crust: Its composition and evolution. *J. Geol.* **1985**, *94*, 57–72.
53. Hofmann, A.W.; Jochum, K.P.; Seufert, M.; White, W.M. Nb and Pb in oceanic basalts: New constraints on mantle evolution. *Earth Planet. Sci. Lett.* **1986**, *79*, 33–45. [[CrossRef](#)]
54. Chappell, B.W.; White, A.J.R. Two contrasting granite types: 25 years later. *Aust. J. Earth Sci.* **2001**, *48*, 489–499. [[CrossRef](#)]
55. Whalen, J.B.; Currie, K.L.; Chappell, B.W. A-type granites: Geochemical characteristics, discrimination and petrogenesis. *Contrib. Mineral. Petrol.* **1987**, *95*, 407–419. [[CrossRef](#)]
56. Barbarin, B. A review of the relationships between granitoid types, their origins, and their geodynamic environments. *Lithos* **1999**, *46*, 605–626. [[CrossRef](#)]
57. Watson, E.B.; Harrison, T.M. Zircon saturation revisited: Temperature and composition effects in a variety of crustal magma types. *Earth Planet. Sci. Lett.* **1983**, *64*, 295–304. [[CrossRef](#)]
58. Eby, G.N. The A-type granitoids: A review of their occurrence and chemical characteristics and speculations on their petrogenesis. *Lithos* **1990**, *26*, 115–134. [[CrossRef](#)]
59. Eby, G.N. Chemical subdivision of the A-type granitoids: Petrogenetic and tectonic implications. *Geology* **1992**, *20*, 641–644. [[CrossRef](#)]
60. Skjerlie, K.P.; Johnston, A.D. Vapor-absent melting at 10 kbar of a biotite- and amphibole-bearing tonalitic gneiss: Implications for the generation of A-type granites. *Geology* **1992**, *20*, 263–266. [[CrossRef](#)]
61. Xin, W.; Sun, F.Y.; Li, L.; Yan, J.M.; Zhang, Y.T.; Wang, Y.C.; Shen, T.S.; Yang, Y.J. The Wulonggou Metaluminous A2-Type Granites in the Eastern Kunlun Orogenic Belt, NW China: Rejuvenation of Subduction-Related Felsic Crust and Implications for Post-Collision Extension. *Lithos* **2018**, *312–313*, 108–127. [[CrossRef](#)]
62. Defant, M.J.; Drummond, M.S. Derivation of some modern arc magmas by melting of young, subducted lithosphere. *Nature* **1990**, *347*, 662–665. [[CrossRef](#)]
63. Defant, M.J.; Xu, J.F.; Kepezhinskas, P.; Wang, Q.; Zhang, Q.; Xiao, L. Adakites: Some variations on a theme. *Acta Petrol. Sin.* **2002**, *18*, 129–142.
64. Martin, H. Adakitic magmas: Modern analogues of Archaean granitoids. *Lithos* **1999**, *46*, 411–429. [[CrossRef](#)]
65. Wang, Q.; Wyman, D.A.; Xu, J.; Jian, P.; Zhao, Z.; Li, C.; Xu, W.; Ma, J.; He, B. Early Cretaceous adakitic granites in the Northern Dabie Complex, central China: Implications for partial melting and delamination of thickened lower crust. *Geochim. Cosmochim. Acta* **2007**, *71*, 2609–2636. [[CrossRef](#)]
66. Gao, S.; Rudnick, R.L.; Yuan, H.L.; Liu, X.M.; Liu, Y.S.; Xu, W.L.; Ling, W.L.; Ayers, J.; Wang, X.C.; Wang, Q.H. Recycling lower continental crust in the North China craton. *Nature* **2004**, *432*, 892–897. [[CrossRef](#)]
67. Hou, Z.Q.; Gao, Y.F.; Qu, X.M.; Rui, Z.Y.; Mo, X.X. Origin of adakitic intrusives generated during mid-Miocene east-west extension in southern Tibet. *Earth Planet. Sci. Lett.* **2004**, *220*, 139–155. [[CrossRef](#)]
68. Atherton, M.P.; Petford, N. Generation of sodium-rich magmas from newly underplated basaltic crust. *Nature* **1993**, *36*, 144–146. [[CrossRef](#)]
69. Wang, Q.; McDermott, F.; Xu, J.F.; Bellon, H.; Zhu, Y.T. Cenozoic K-rich adakitic volcanic rocks in the Hohxil area, northern Tibet: Lower-crustal melting in an intracontinental setting. *Geology* **2005**, *33*, 465–468. [[CrossRef](#)]
70. Castillo, P.R.; Janney, P.E.; Solidum, R.U. Petrology and geochemistry of Camiguin Island, southern Philippines: Insights to the source of adakites and other lavas in a complex arc setting. *Contrib. Mineral. Petrol.* **1999**, *134*, 33–51. [[CrossRef](#)]
71. Wareham, C.D.; Millar, L.L.; Vaughan, A.P.M. The generation of sodic granite magmas, western Palmer Land, Antarctic Peninsula. *Contrib. Mineral. Petrol.* **1997**, *128*, 81–96. [[CrossRef](#)]
72. Stern, C.R.; Kilian, R. Role of the subducted slab, mantle wedge and continental crust in the generation of adakites from the Andean Austral Volcanic Zone. *Contrib. Mineral. Petrol.* **1996**, *123*, 263–281. [[CrossRef](#)]
73. Xu, H.; Ma, C.; Zhang, J. Generation of Early Cretaceous High-Mg adakitic host and enclaves by magma mixing, Dabie Orogen, Eastern China. *Lithos* **2012**, *142–143*, 182–200. [[CrossRef](#)]
74. Pearce, J.A.; Harris, N.B.W.; Tindle, A.G. Trace element discrimination diagrams for the tectonic interpretation of granitic rocks. *J. Petrol.* **1984**, *25*, 956–983. [[CrossRef](#)]
75. Wu, F.Y.; Tang, J.H.; Liu, X.M. Geochronological Framework of the Mesozoic Granitic Magmatism in the Liaodong Peninsula, Northeast China. *Geol. J. China Univ.* **2005**, *11*, 305–317. (In Chinese)
76. Peng, Y.J.; Qi, C.D.; Zhou, X.D.; Lu, X.B.; Dong, H.C.; Li, Z. Transition from Paleo-Asian Ocean domain to circum-pacific ocean domain for the Ji-Hei composite orogenic belt: Time mark and relationship to global tectonics. *Geol. Resour.* **2012**, *21*, 261–265. (In Chinese with English Abstract)
77. Yu, Q.; Ge, W.C.; Yang, H.; Zhao, G.C.; Zhang, Y.L.; Su, L. Petrogenesis of late Paleozoic volcanic rocks from the Daheshen Formation in central Jilin Province, NE China, and its tectonic implications: Constraints from geochronology, geochemistry and Sr-Nd-Hf isotopes. *Lithos* **2014**, *192–195*, 116–131. [[CrossRef](#)]

78. Zhao, J.; Peng, Y.J.; Ding, M.G.; Liu, D.Y.; Zhang, N.; Yang, C. Late Hercynian–early indosinian magmatic cycles in Meihekou–Kaiyuan between Jilin and Liaoning provinces: Tectonic implication. *Geol. Resour.* **2012**, *21*, 371–375. (In Chinese with English Abstract)
79. Wu, F.Y.; Zhao, G.C.; Sun, D.Y.; Wilde, S.A.; Yang, J.H. The Hulan Group: Its role in the evolution of the Central Asian Orogenic Belt of NE China. *J. Asian Earth Sci.* **2007**, *30*, 542–556. [[CrossRef](#)]
80. Feng, G.Y.; Liu, S.; Zhong, H.; Jia, D.C.; Qi, Y.Q.; Wang, T.; Yang, Y.H. Geochemical characteristics and petrogenesis of late Paleozoic mafic rocks from Yumuchuan, Jilin Province. *Geochimica* **2010**, *39*, 427–438. (In Chinese with English Abstract)
81. Chen, Q.; Qiu, G.L.; Xue, L.F.; Zou, X.M.; Zhou, H.P.; Du, Y.S. Palaeoplate evolution in the southern part of the Inner Mongolian Orogenic belt. *Geol. Rev.* **1993**, *39*, 477–483. (In Chinese with English Abstract)
82. Ma, S.X.; Wang, Z.Q.; Zhang, Y.L.; Sun, J.X. Bainaimiao Arc as an Exotic Terrane Along the Northern Margin of the North China Craton: Evidences from Petrography, Zircon U–Pb Dating, and Geochemistry of the Early Devonian Deposits. *Tectonics* **2019**, *38*, 2606–2624. [[CrossRef](#)]
83. Shang, H.S.; Tao, J.X.; Bao, Y.W.L.J.; Hao, X.Y. The arc–basin system and tectonic significance of early Paleozoic in Baiyunebo area, Inner Mongolia. *Geol. Surv. Res.* **2003**, *26*, 160–168. (In Chinese with English Abstract)
84. Shao, J.A. The early Paleozoic ophiolite in central Nei Mongol and its significance in revealing the evolution history of the crust. In *Contributions to the Project of Plate Tectonics in Northern China*; Tang, K.D., Ed.; Geological Publishing House: Beijing, China, 1986; Volume 1, pp. 158–172.
85. Tian, Y.J.; Xu, B.; Zhang, Y.J.; Yang, Z.N.; Yao, Z.W. Sedimentary Facies and Provenance Area Analysis of Xuniwusu Formation in Tugurige Area, Southern Xing-Meng Orogenic Belt and Their Tectonic Significance. *Acta Sci. Nat. Univ. Pekin.* **2019**, *55*, 1038–1054. [[CrossRef](#)]
86. Zhang, J.F.; Liu, Z.H.; Guan, Q.B.; Xu, Z.Y.; Wang, X.A.; Zhu, K. Age, and geological significance of Xuniwusu Formation from Bainaimiao area of Sonid Youqi, Inner Mongolia. *Acta Petrol. Sin.* **2017**, *33*, 3147–3160.
87. Fu, C.L.; Sun, D.Y.; Zhang, X.Z.; Wei, H.Y.; Gou, J. Discovery and geological significance of the Triassic high–Mg diorites in Hunchu area. Jilin Province. *Acta Petrol. Sin.* **2010**, *26*, 1089–1102. (In Chinese with English Abstract)
88. Yuan, L.L.; Zhang, X.H.; Xue, F.H.; Lu, Y.H.; Zong, K.Q. Late Permian High-Mg andesite and basalt association from northern Liaoning, North China: Insights into the final closure of the Paleo-Asian Ocean and the orogen-craton boundary. *Lithos* **2016**, *258*, 58–76. [[CrossRef](#)]